ELSEVIER

A micromechanical continuum model for the tensile behavior of shape memory metal nanowires

Wuwei Liang[a], David J. Srolovitz[b], Min Zhou[a],*

[a]*George W. Woodruff School of Mechanical Engineering, Georgia Institute of Technology, Atlanta, GA 30332, USA*
[b]*Department of Physics, Yeshiva University, New York, NY 10033, USA*

Abstract

We have previously discovered a novel shape memory effect and pseudoelastic behavior in single-crystalline face-centered-cubic metal (Cu, Ni, and Au) nanowires. Under tensile loading and unloading, these wires can undergo recoverable elongations of up to 50%, well beyond the recoverable strains of 5–8% typical for most bulk shape memory alloys. This phenomenon only exists at the nanoscale and is associated with a reversible lattice reorientation driven by the high surface-stress-induced internal stresses. We present here a micromechanical continuum model for the unique tensile behavior of these nanowires. Based on the first law of thermodynamics, this model decomposes the lattice reorientation process into two parts: a reversible, smooth transition between a series of phase-equilibrium states and a superimposed irreversible, dissipative twin boundary propagation process. The reversible part is modeled within the framework of strain energy functions with multiple local minima. The irreversible, dissipative nature of the twin boundary propagation is due to the ruggedness of strain energy curves associated with dislocation nucleation, glide, and annihilation. The model captures the major characteristics of the unique behavior due to lattice reorientation and accounts for the size and temperature effects, yielding results that are in excellent agreement with the results of molecular dynamics simulations.

Keywords: Shape memory effect; Pseudoelasticity; Nanowires; Micromechanical continuum model; Lattice reorientation

*Corresponding author. Tel.: +1 404 894 3294; fax: +1 404 894 0186.
  E-mail address: min.zhou@gatech.edu (M. Zhou).

1. Introduction

Until recently, the shape memory effect (SME) and its underlying pseudoelasticity were considered unique to shape memory alloys (SMAs), liquid crystal elastomers, and piezoelectric ceramics (Otsuka and Wayman, 1998). However, our recent research revealed a novel SME and rubber-like pseudoelastic behavior in single-crystalline metal nanowires (including Cu and Ni) with cross-sectional dimensions smaller than approximately 5 nm (Liang and Zhou, 2005, 2006; Liang et al., 2005). Specifically, under tensile loading and unloading, these nanowires can recover elongations of up to 50%, well beyond the recoverable strains of 5–8% typical for most bulk SMAs. This behavior is associated with a reversible lattice reorientation process within the face-centered cubic (FCC) crystalline structure and is driven by the surface stress and high surface-to-volume ratios of these quasi one-dimensional nanomaterials. This novel shape memory behavior of metal nanowires has also been confirmed by the research of Park et al. (2005) and Park and Ji (2006).

Due to the lattice reorientation, the nanowires exhibit a unique tensile behavior under isothermal, quasi-static conditions, as shown in Fig. 1. The principal interest of this paper is to develop a micromechanical continuum model for this unique tensile behavior based on detailed analysis of the deformation mechanisms. In particular, the model focuses on the lattice reorientation that occurs through twin boundary propagation. As will be discussed in the next section, this reversible lattice reorientation involves two wire configurations: the initial $\langle 1\,1\,0 \rangle/\{1\,1\,1\}$ configuration with a $\langle 1\,1\,0 \rangle$ wire axis and $\{1\,1\,1\}$ surfaces and the deformed $\langle 0\,0\,1 \rangle/\{1\,0\,0\}$ configuration with a $\langle 0\,0\,1 \rangle$ wire axis and $\{1\,0\,0\}$ surfaces, as shown in Fig. 2. Although both wire configurations have the same FCC structure, the $\langle 1\,1\,0 \rangle/\{1\,1\,1\}$ wires have lower strain energy levels than the $\langle 0\,0\,1 \rangle/\{1\,0\,0\}$ configurations primarily because $\{1\,1\,1\}$ surfaces have lower energies than $\{1\,0\,0\}$ surfaces. Since the surface-to-volume ratios of nanowires are very large, surface energies dominate the strain energy difference between different nanowire configurations (discussed in Section 3.2). Because the different wire configurations have different strain energies and stabilities, we treat them as two phases in the following discussion. Accordingly, the lattice reorientation process can be modeled as a phase transformation.
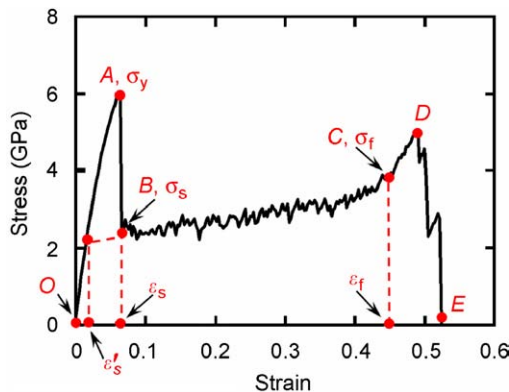

Fig. 1. Stress–strain curve of a FCC nanowire under isothermal quasi-static tensile deformation.
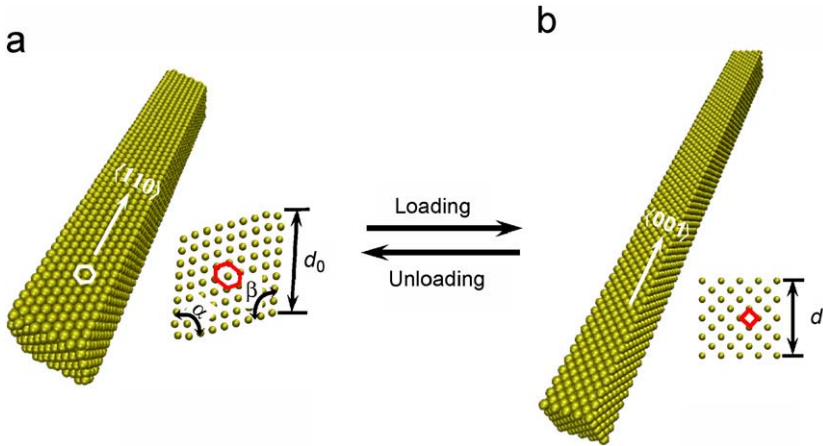
Fig. 2. Pseudoelastic behavior of metal nanowires: (a) a self-equilibrated $\langle 1\,1\,0 \rangle/\{1\,1\,1\}$ wire with rhombic cross-sections ($\alpha = 70.5°$ and $\beta = 109.5°$) and (b) a stretched $\langle 0\,0\,1 \rangle/\{1\,0\,0\}$ wire with square cross-section.

Before proceeding to more details, we would like to clarify the definition of the aforementioned strain energy, because it is critical for the development of the model and will be frequently used in this paper. In continuum mechanics, strain energy is usually defined as the potential energy stored in a body by virtue of an elastic deformation, equal to the work that must be done to produce the deformation (Parker, 2002). The strain energy in this paper includes not only the potential energy associated with bulk elastic deformation, but also the surface energy, reflecting the fact that the surface energy is due to the elastic deformation of atomic lattices on and near surfaces. More generally, the strain energy of a nanowire here is defined as the excessive potential energy it possesses relative to its potential energy as part of an infinitely large bulk material in equilibrium at a given temperature. If the wire size is very large (approaching microns or even higher), the surface energy is negligible compared to the bulk potential energy. At the nanoscale, however, the surface energy is significant and even dominates the total strain energy. More discussions regarding the total strain energy and its surface and bulk components in nanowires will be given in Section 3.2.

We found that this lattice reorientation process is dissipative even as the deformation rate tends to zero (i.e., quasi-static conditions). In this study, this lattice reorientation process is decomposed into a non-dissipative part and a superimposed dissipative part. The non-dissipative part describes the smooth transition between a series of phase-equilibrium states; i.e., an ideal and thermodynamically reversible process. The dissipative part is the process of twin boundary propagation, which involves passing over the energy barriers between phase-equilibrium states—a thermodynamically irreversible process. Since the $\langle 1\,1\,0 \rangle/\{1\,1\,1\}$ and $\langle 0\,0\,1 \rangle/\{1\,0\,0\}$ configurations each correspond to a local energy minimum in the strain energy of nanowires under tensile elastic deformation, the reversible part is modeled within the framework of strain energy functions with multiple local minima (Abeyaratne and Knowles, 1993; Abeyaratne and Kim, 1994; Abeyaratne and Vedantam, 2003). Specifically, at any given strain, the wire adopts the configuration that minimizes the strain energy, subject to the appropriate kinematic constraints and force balance. Although this framework has been very successful in modeling static

phase-equilibrium states, there are some practical difficulties in modeling dynamic and quasi-static processes, primarily due to the lack of an accurate kinetic law for phase boundary propagation. Since our interest is in the quasi-static process, we do not attempt to explicitly calculate the driving force or derive an explicit kinetic law to determine the relationship between the driving force and phase boundary propagation velocity. Instead, we study the source of energy dissipation by performing a detailed analysis of the lattice scale deformation mechanism. Specifically, the energy dissipation is derived from the rugged strain energy landscape associated with dislocation nucleation, propagation, and annihilation during twin boundary propagation.

The organization of this paper is as follows: Section 2 introduces the novel SME and pseudoelastic behavior of nanowires. Specifically, the tensile behavior is partitioned into four stages based upon the underlining deformation mechanisms. The focus is on the lattice reorientation process, which is critical to the shape memory behavior of nanowires. Section 3 briefly introduces the theory of strain energy functions with multiple local minima for modeling phase transformations. The strain energy and stability of nanowires are also analyzed with an emphasis on the dominance of surface energies. In Section 4, we present a piecewise smooth model with each piece corresponding to one deformation stage. In Section 5, the model predictions are compared with the results of molecular dynamics (MD) simulations. We demonstrate that the model accurately captures the major characteristics of the unique tensile behavior associated with the lattice reorientation process observed in the MD simulations, as well as the major characteristics of the observed size and temperature effects. We summarize our results in Section 6.

2. Novel shape memory behavior of metal nanowires

The shape memory metal nanowires are single FCC crystals with a $\langle 1\,1\,0 \rangle$ axis and $\{1\,1\,1\}$ transverse surfaces (hereafter denoted as the $\langle 1\,1\,0 \rangle/\{1\,1\,1\}$ wire or configuration) in their unstressed free-standing states, as shown in Fig. 2(a). This configuration represents a low-energy state for FCC metal nanowires and has been observed frequently in experiments and atomistic simulations for Au, Cu, and Ag nanowires (Kondo and Takayanagi, 1997; Liu and Bando, 2003; Liu et al., 2003; Rodrigues and Ugarte, 2003; Diao et al., 2004a, b). Upon isothermal, quasi-static, tensile deformation, these $\langle 1\,1\,0 \rangle/\{1\,1\,1\}$ wires exhibit a stress–strain behavior that is drastically different from those of the corresponding bulk metals, as shown in Fig. 1. Specifically, the stress–strain curves consists of two elastic deformation stages (O→A and C→D), an intervening stage of slow "strain hardening" over a wide range of strain (B→C), and two stages of precipitous stress drop (A→B and D→E). This behavior arises from a unique underlining deformation process:

(1) between O and A the $\langle 1\,1\,0 \rangle/\{1\,1\,1\}$ wire undergoes elastic stretching,
(2) the load drop between A and B corresponds to the formation of one twin boundary,
(3) point A corresponds to the beginning of the lattice reorientation process which leads to the new $\langle 0\,0\,1 \rangle/\{1\,0\,0\}$ configuration (see Fig. 2(b)) at point C in Fig. 1,
(4) between C and D, the newly formed $\langle 0\,0\,1 \rangle/\{1\,0\,0\}$ wire undergoes elastic stretching, and
(5) further loading beyond D causes the wire to yield through the formation of full dislocations which ultimately lead to necking and fracture of the nanowire at E (Liang and Zhou, 2004).

The unique lattice reorientation process (A→C in Fig. 1) is the key to the pseudoelastic behavior and SME of the wires because it is reversible upon unloading. This lattice reorientation occurs through the propagation of a coherent twin boundary separating the initial $\langle 1\,1\,0\rangle/\{1\,1\,1\}$ phase and the new $\langle 0\,0\,1\rangle/\{1\,0\,0\}$ phase, as shown in Fig. 3. The twin boundary propagates in a "stick–slip" manner through successive dislocation nucleation, glide, and annihilation events, which are the source of energy dissipation—no matter how slow the deformation progresses (Vainchtein and Rosakis, 1999). As the twin boundary sweeps through the wire, the wire progressively transforms into the new $\langle 0\,0\,1\rangle/\{1\,0\,0\}$ phase. Upon arrival of the twin boundary at the far end of the wire (corresponding to point C in Fig. 1), the whole wire is in the $\langle 0\,0\,1\rangle/\{1\,0\,0\}$ phase (Liang et al., 2005; Liang and Zhou, 2006).

Upon unloading above a critical temperature, the $\langle 0\,0\,1\rangle/\{1\,0\,0\}$ wire spontaneously transforms back to the original $\langle 1\,1\,0\rangle/\{1\,1\,1\}$ configuration via a lattice reorientation process that is the reverse of that described above for loading. The reversibility of the lattice reorientation from $\langle 1\,1\,0\rangle/\{1\,1\,1\}$ to $\langle 0\,0\,1\rangle/\{1\,0\,0\}$ allows the associated deformation to be fully recovered, giving rise to the pseudoelastic behavior of the wire. This spontaneous lattice reorientation occurs because the $\langle 1\,1\,0\rangle/\{1\,1\,1\}$ configuration has a lower total energy and is more stable than the $\langle 0\,0\,1\rangle/\{1\,0\,0\}$ configuration. Therefore, the $\langle 0\,0\,1\rangle/\{1\,0\,0\}$ wire has a natural tendency for spontaneous reorientation back to the
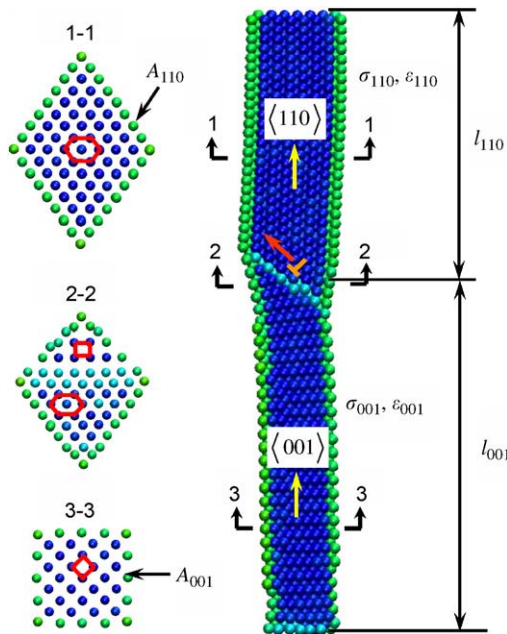

Fig. 3. Cross-sections of a $1.96 \times 1.96\,\text{nm}$ Cu wire at a strain of 0.24. The right image shows a sectional view along the wire axis and the $[\bar{1}\,\bar{1}\,0]$ diagonal of the cross-section: cross-section 1-1 shows the elongated hexagonal lattice in the unrotated domain with the $\langle 1\,0\,0\rangle/\{1\,1\,1\}$ phase, cross-section 2-2 is in the transition region containing both the $\langle 0\,0\,1\rangle/\{1\,0\,0\}$ and the $\langle 1\,1\,0\rangle/\{1\,1\,1\}$ phases, and cross-section 3-3 shows the square lattice in the reoriented domain with the $\langle 0\,0\,1\rangle/\{1\,0\,0\}$ phase, the atoms are colored by centrosymmetry values.

$\langle 1\,1\,0 \rangle / \{1\,1\,1\}$ configuration upon removal of the load. This reverse reorientation lowers the surface energy of the system, since the $\{1\,0\,0\}$ surfaces have higher energy than the $\{1\,1\,1\}$ surfaces. Crudely, this is because the $\{1\,1\,1\}$ surfaces are close-packed while the $\{1\,0\,0\}$ surfaces have a relatively low atomic density. While this provides the thermodynamic driving force for the transformation, the motion of the individual dislocations that translate the twin boundary are driven by the Peach–Koehler force associated with stresses within the wire. In the absence of an applied load, the tensile surface stress produces a compressive stress within the wire. While this stress is typically very small in bulk materials, the fact that it scales inversely with the linear dimension of the wire cross-section leads to very large stresses (on the order of GPa here (Liang and Zhou, 2005)) due to the extremely large surface-to-volume ratios in nanowires. This is one of the reasons why SME and pseudoelastic behavior are not seen in bulk single crystals of these metals.

Like the behavior of normal bulk SMAs, the spontaneous lattice reorientation is strongly temperature-dependent. Specifically, the reverse lattice reorientation from $\langle 0\,0\,1 \rangle$ to $\langle 1\,1\,0 \rangle$ occurs only above a size-dependent critical temperature T_{cr}. If unloading takes place at temperatures below T_{cr}, the reverse lattice reorientation does not occur and the wire retains the $\langle 0\,0\,1 \rangle / \{1\,0\,0\}$ configuration. When subsequently heated above T_{cr}, the unloaded $\langle 0\,0\,1 \rangle / \{1\,0\,0\}$ wire spontaneously returns to its original $\langle 1\,1\,0 \rangle / \{1\,1\,1\}$ configuration through the reverse lattice reorientation. This is a novel SME driven by surface stress and the high surface-to-volume ratios of the nanowire. The observed temperature-dependence is related to the energy barrier between the two phases and the driving force required to cross it. To initiate the reorientation, partial dislocations nucleate and propagate to move the twin boundary. There is an additional barrier associated with the nucleation of the partial dislocations. Thermal vibration can provide the necessary energy for overcoming the barrier (Meyers, 1984).

Compared to bulk SMAs, the shape memory nanowires have extraordinarily large reversible strains (up to 50%) primarily due to the large transformation strain ($\varepsilon_{\mathrm{tr}}$) associated with the forward and reverse lattice reorientations. Specifically, $\varepsilon_{\mathrm{tr}}$ can be quantified by a simple crystallographic analysis. Fig. 4 compares the same $(1\,\bar{1}\,0)$ plane in the $\langle 1\,1\,0 \rangle / \{1\,1\,1\}$ (at point A in Fig. 1) and the $\langle 0\,0\,1 \rangle / \{1\,0\,0\}$ configurations (at point C in Fig. 1). Clearly, the forward (loading) and backward (unloading) lattice reorientations manifest as $90°$ rotations in opposite directions of the unit cell in the $(1\,\bar{1}\,0)$ plane. The length and width of the rectangular unit cell in both cases are, respectively, a and $\frac{\sqrt{2}}{2}a$; where a is the lattice constant in the stressed states and is assumed to be the same at A and C. Hence, the axial strain associated with the lattice reorientation between A and C is given by

$$\varepsilon_{\mathrm{tr}} = \left(a - \frac{\sqrt{2}}{2}a \right) \Big/ \frac{\sqrt{2}}{2}a = 0.414. \tag{1}$$

Clearly, $\varepsilon_{\mathrm{tr}}$ is an attribute of the FCC structure and is independent of a. Consequently, the pseudoelastic strain associated with the lattice reorientation which constitutes the primary part of the total recoverable strain (ε_{r}) is the same for wires of all FCC metals and of all sizes. In addition to $\varepsilon_{\mathrm{tr}}$, ε_{r} also includes the elastic strain $\varepsilon^{\mathrm{e}}_{(1\,1\,0)}$ associated with the lattice stretching in the $\langle 1\,1\,0 \rangle / \{1\,1\,1\}$ configuration between O and A (Fig. 1) and the elastic strain $\varepsilon^{\mathrm{e}}_{(0\,0\,1)}$ associated with the lattice stretching in the $\langle 0\,0\,1 \rangle / \{1\,0\,0\}$
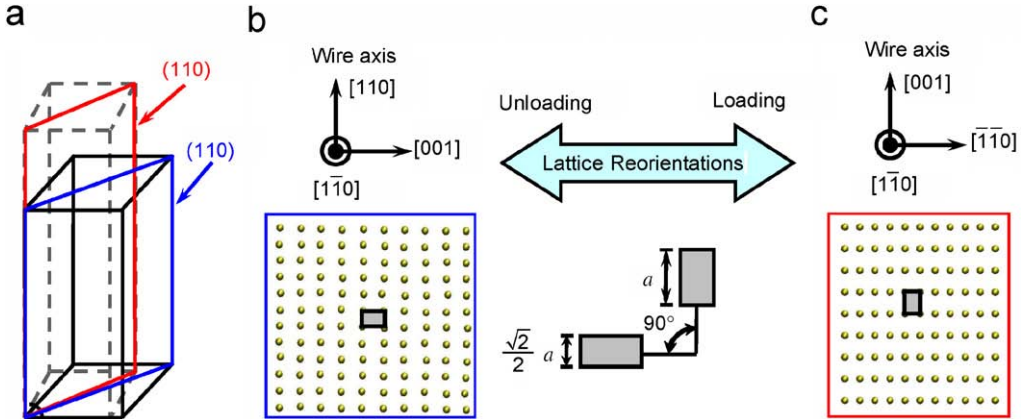
Fig. 4. Reversible lattice reorientations upon loading and unloading in metal nanowires; (a) a schematic illustration of the wire configurations before and after lattice reorientation, (b) the $(1\bar{1}0)$ atomic plane highlighted in blue in (a), and (c) the same $(1\bar{1}0)$ atomic plane after lattice reorientation highlighted in red in (a).

configuration between C and D, i.e.,

$$\varepsilon_r \approx \varepsilon^e_{\langle 1\,1\,0\rangle} + \varepsilon_{tr} + \varepsilon^e_{\langle 0\,0\,1\rangle}. \tag{2}$$

Overall, ε_r is ~50%, well beyond the 5–8% reversible strains typical for most bulk SMAs.

3. Phase transformation model based upon strain energy functions

This section briefly introduces the theory of strain energy functions with multiple local minima for modeling of phase transformations. The strain energy functions of nanowires are also analyzed with an emphasis on the dominance of surface energies.

3.1. Theory of strain energy functions with multiple local minima

With regard to the modeling of phase transformations, Abeyarantne et al. presented a theoretical framework of strain energy functions with multiple local minima, where each local energy minimum corresponds to a phase or variant of the material (Abeyaratne and Knowles, 1993; Abeyaratne and Kim, 1994; Abeyaratne and Vedantam, 2003). As the load is varied, the relative stability of each phase changes and the less stable phase transforms into the more stable phase through the propagation of the phase boundary. The initiation of the phase transformation is governed by a nucleation condition, and the rate of transformation or how fast the phase boundary propagates is governed by a kinetic law. In this framework, a thermodynamics driving force is defined by the states at the vicinity of the phase boundary. For example, in one-dimension:

$$f = [\![w]\!] - \langle\sigma\rangle[\![\varepsilon]\!], \tag{3}$$

where $[\![w]\!]$ denotes the jump of strain energy density across the phase boundary, $\langle\sigma\rangle$ denotes the average stress in the vicinity of the phase boundary, and $[\![\varepsilon]\!]$ denotes the strain

jump across the phase boundary. The kinetic law determines the relation between the velocity of the phase boundary (v) and the driving force (f), i.e.,

$$f = \varphi(v), \tag{4}$$

where f must satisfy the dissipation inequality associated with the phase boundary propagation in the form of

$$f\,v \geqslant 0. \tag{5}$$

The preceding framework has been successful in modeling martensitic transformations in bulk SMAs, especially for static problems. However, one difficulty with this framework is the construction of accurate strain energy functions. Many strain energy functions can only qualitatively capture the characteristics of the phase transformation, but fail to provide quantitatively accurate models, primarily because of the restrictive nature of the kinematic constraints (Abeyaratne et al., 2001). Moreover, there are more difficulties in using the preceding framework for dynamic problems, e.g., the lack of an accurate kinetic law and quantitative information on energy dissipation. Accurate kinetic laws are difficult to obtain because they are unrestricted by continuum theory except by the necessity of having to satisfy the dissipation inequality. Usually, microscopic (e.g., lattice-based) models are required to analyze the many factors that determine the kinetic laws (Abeyaratne and Knowles, 1991). The dissipation inequality only implies that the energy dissipation must be greater than zero, but it does not give any quantitative information. Nonetheless, even the quasi-static phase transformation process has to be analyzed as a dynamic process because the driving force $f \neq 0$.

To avoid the difficulties in the analysis of dynamic processes within the preceding framework, the present model decomposes the quasi-static lattice reorientation process into a smooth transition between a series of static phase-equilibrium states superimposed with a phase boundary propagation process based on the first law of thermodynamics. After the decomposition, each of the phase-equilibrium states in the smooth transition can be studied individually as a static problem. And the energy dissipation associated with the phase boundary propagation can be analyzed independently.

Specifically, the static phase-equilibrium problem is studied by constrained strain energy minimization within the preceding framework without the necessity of kinetic laws. Instead of constructing the complete strain energy functions over a full 3D strain space, we only consider the 1D strain energy function because of the near 1D nature of the wire structure and the 1D nature of the uniaxial tensile deformation. Moreover, we neglect the portion of the strain energy function corresponding to unstable states and only use the portion of the strain energy functions around the local energy minima, where phases are stable. To state it more precisely, we only consider strain energy functions corresponding to the elastic deformations of the two pure phases involved in lattice reorientation. Therefore, an accurate strain energy function can be easily obtained from experiments, MD simulations, and even analytical expressions (as discussed in the next subsection) based upon bulk and surface elastic constants. Since the strain energy functions of the pure phases already account for the significant surface energies in nanowires, the model automatically accounts for the size dependence of this behavior.

3.2. Strain energy of nanowires

The $\langle 1\,1\,0\rangle/\{1\,1\,1\}$ and $\langle 0\,0\,1\rangle/\{1\,0\,0\}$ wire configurations have different elastic constants and strain energies when subject to the same elastic deformation, even though both configurations are FCC. The strain energies of these two phases are critical to the lattice reorientation because the strain energies determine the relative stability of the two phases.

Compared to the strain energy of bulk materials, the strain energy of nanowires is not only a function of strain, but also the wire size. Furthermore, the strain energy of a nanowire does not go to zero in the zero strain limit. These special characteristics originate in the large surface-to-volume ratio of nanowires. We know atoms on or near a free surface have different energies from those in the bulk because surface atoms experience a different local environment from those in the bulk of a material. Such surface effects are usually insignificant and negligible in bulk materials because the number of surface atoms is small compared to the total number of atoms. However, these surface effects can be substantial for nanowires because of the extremely large surface-to-volume ratios. For example, the surface-to-volume ratio of a 1.8×1.8 nm nanowire is 10^6 times larger than that of a typical macroscopic tensile specimen which has a cross-sectional dimension of 1.8×1.8 mm (Liang and Zhou, 2005). The surface energy constitutes a significant portion of the total strain energy of the wire. Taking surface energies into account, the strain energy of nanowires can be written in the following form (Streitz et al., 1994; Cammarata et al., 2000; Dingreville et al., 2005):

$$U = U_{\text{bulk}} + U_{\text{surface}}, \tag{6}$$

where U_{bulk} is the strain energy in the bulk of the wire, and U_{surface} the surface energy. Specifically the strain energy for a $\langle 1\,1\,0\rangle/\{1\,1\,1\}$ wire with lateral size d_0 and length l_0 (see Fig. 2(a)) is

$$U_{1\,1\,0} = u_{1\,1\,0}(\varepsilon)l_0 d_0^2 \sin\alpha + 4\gamma_{1\,1\,1}(\varepsilon)l_0 d_0, \tag{7}$$

where $u_{110}(\varepsilon)$ is the strain energy of a bulk material stretched in the $\langle 1\,1\,0\rangle$ orientation, $\alpha = 70.5°$ is the sharp angle of the rhombic cross-section, and $\gamma_{111}(\varepsilon)$ is the surface energy of $\{1\,1\,1\}$ surfaces. Similarly, the strain energy for a $\langle 0\,0\,1\rangle/\{1\,0\,0\}$ wire with lateral size d and length l (see Fig. 2(b)) is

$$U_{001} = u_{001}(\varepsilon)ld^2 + 4\gamma_{100}(\varepsilon)ld, \tag{8}$$

where $u_{001}(\varepsilon)$ is the strain energy of a bulk material stretched in the $\langle 0\,0\,1\rangle$ orientation and $\gamma_{100}(\varepsilon)$ the surface energy of $\{1\,0\,0\}$ surfaces. Fig. 5(a) shows the total strain energy and its two components, U_{bulk} and U_{surface}, for a 1.45×1.45 nm $\langle 0\,0\,1\rangle/\{1\,0\,0\}$ wire. Clearly, U_{surface} dominates the total strain energy due to the extremely high surface-to-volume ratios.

We can also see that the minimum strain energy point, which corresponds to the unstressed self-equilibrium state, is at a compressive strain (Dingreville et al., 2005). This compressive strain, in the self-equilibrium state, is induced by surface stress in the nanowire (assuming the most common situation, where the surface stress is tensile). Consider a wire cut from a bulk; the wire will contract along the axial direction and expand in the lateral directions because of the tensile surface stresses (assuming a positive Poisson ratio), as shown in Fig. 5(b). The axial contraction causes a compressive stress σ in the core
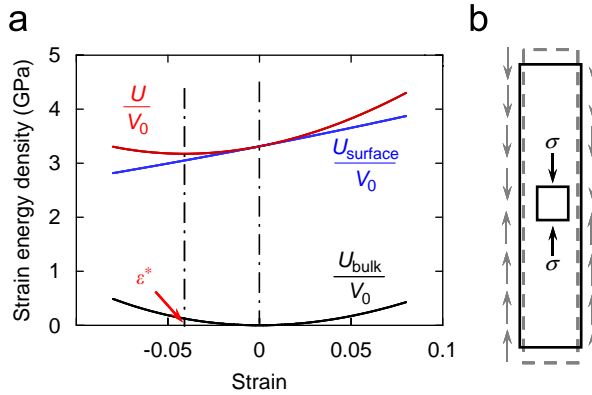
Fig. 5. (a) The strain energy density function and its bulk and surface components of a 1.9×1.9 nm $\langle 0\,0\,1 \rangle/$ $\{1\,0\,0\}$ Cu wire, the reference state is the undeformed bulk lattice. (b) A schematic illustration of the contraction of a wire under surface stress.

of the wire, which is balanced by the tensile surface stress in the equilibrium state. The magnitude of σ is inversely proportional to the lateral size of the wire. In a nanowire, σ can easily be of the order of 1 GPa. In contrast, σ is only on the order of Pascals in bulk materials and thus is negligible.

The self-equilibrium strain ε^* can be obtained analytically by minimizing the strain energy in Eq. (6),

$$\left.\frac{\partial U}{\partial \varepsilon}\right|_{\varepsilon=\varepsilon^*} = 0. \tag{9}$$

In MD simulations, ε^* can be obtained by simulating a top–down nanowire fabrication process, which involves cutting a wire from bulk and relaxing the wire at a constant temperature until it reaches the self-equilibrium state. ε^* can then be calculated from the original length and the length in the self-equilibrium state.

ε^* is related to wire size and configurations (wire axis orientation and transverse surfaces). For the wires of the same dimensionless shape, ε^* is smaller in larger wires. For wires of the same size, ε^* in $\langle 1\,1\,0 \rangle/\{1\,1\,1\}$ wires is smaller than that in $\langle 0\,0\,1 \rangle/\{1\,0\,0\}$ wires. For example, ε^* is equal to 0.02 and 0.04, respectively, for a 1.8×1.8 nm $\langle 1\,1\,0 \rangle/$ $\{1\,1\,1\}$ Cu wire and the corresponding $\langle 0\,0\,1 \rangle/\{1\,0\,0\}$ wire at 300 K.

In calculating ε^*, we have used the undeformed bulk lattices as the reference states to show the axial contraction under surface stress. However, in the following discussions, we use the unloaded self-equilibrium states as the reference states of the wires unless otherwise indicated. With these reference states, the stress is zero at zero strain. Moreover, the wire has the minimum strain energy in its reference state. It is important to point out that the actual strain energy values also depend on the selected ground state. In this study, the ground state is the undeformed bulk lattice and strain energy of nanowires does not equal zero at the reference states. As shown in Fig. 6, the strain energies at the reference states are 2.95 and 3.24 GPa for the $\langle 1\,1\,0 \rangle/\{1\,1\,1\}$ and $\langle 0\,0\,1 \rangle/\{1\,0\,0\}$ phases, respectively. In the next section, a constitutive model will be derived based on the strain energy functions of $\langle 1\,1\,0 \rangle/\{1\,1\,1\}$ and $\langle 0\,0\,0 \rangle/\{1\,0\,0\}$ wires as shown in Fig. 6.
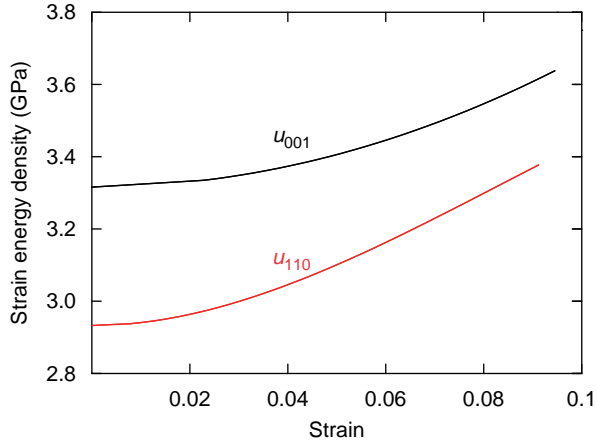
Fig. 6. The strain energy density functions of a 1.96×1.96 nm $\langle 1\,1\,0 \rangle / \{1\,1\,1\}$ Cu wire and the corresponding $\langle 0\,0\,1 \rangle / \{1\,0\,0\}$ wire—the reference states are the unstressed states of the corresponding phases, respectively.

4. Piecewise smooth micromechanical continuum model

As discussed in Section 2, the tensile deformation behavior of wires can be partitioned into four deformation stages according to the underlining deformation mechanisms. We only discuss the first three stages because only their associated deformations are reversible upon unloading. The constitutive model is piecewise smooth with each piece associated with one of the deformation stages. Particularly, this model focuses on the lattice reorientation, because it is this unique deformation mechanism that leads to the novel SME of metal wires with large reversible strains. The model captures the major characteristics of the lattice reorientation process, especially all the critical parameters (see Fig. 1), including

(1) the yield stress σ_y at the initiation of lattice reorientation,
(2) the start and finish strains (ε_s and ε_f) for the lattice reorientation process, and
(3) the stress levels during lattice reorientation, especially the start and finish stresses (σ_s and σ_f).

Before we introduce the model, it is important to clarify the definitions of the different stresses and strains involved in this analysis. The stress σ and strain ε in the stress–strain curve in Fig. 1 are the total nominal stress and nominal strain with the assumption that stresses and strains are uniform throughout the wire, even though the stresses and strains are not necessarily the same in the two phases during lattice reorientation. Specifically, ε is the nominal engineering strain with the initial $\langle 1\,1\,0 \rangle / \{1\,1\,1\}$ wire in its self-equilibrated state as the reference state. Hence, ε is given by

$$\varepsilon = \frac{\delta}{l_0}, \tag{10}$$

where δ is the total displacement and l_0 the length of the initial unstressed $\langle 1\,1\,0 \rangle / \{1\,1\,1\}$ wire at a given temperature. During deformation, the total mechanical work done by

external load is

$$W = V_0 \int_0^\varepsilon \sigma \, d\varepsilon. \tag{11}$$

Accordingly, the average stress σ is given by

$$\sigma = \frac{1}{V_0} \frac{\partial W}{\partial \varepsilon}, \tag{12}$$

where V_0 is the initial wire volume in the unstressed state.

In the following discussions, we also need to consider the local stresses (σ_{110} and σ_{001}) and strains (ε_{110} and ε_{001}) in the $\langle 1\,1\,0 \rangle/\{1\,1\,1\}$ and $\langle 0\,0\,1 \rangle/\{1\,0\,0\}$ phases, respectively, as shown in Fig. 3. Specifically, ε_{110} and ε_{001} are engineering strains with the reference states being the unstressed self-equilibrium states of the $\langle 1\,1\,0 \rangle/\{1\,1\,1\}$ and $\langle 0\,0\,1 \rangle/\{1\,0\,0\}$ phases, respectively. Obviously, σ_{110} and ε_{001} are given by

$$\sigma_{110} = \frac{du_{110}}{d\varepsilon_{110}} \tag{13}$$

and

$$\sigma_{001} = \frac{du_{001}}{d\varepsilon_{001}}, \tag{14}$$

where u_{110} and u_{001} are the strain energy density functions of two phases, as shown in Fig. 6.

4.1. Elastic deformation of the $\langle 1\,1\,0 \rangle/\{1\,1\,1\}$ phase

Initially, the wire is in a single $\langle 1\,1\,0 \rangle/\{1\,1\,1\}$ phase state. Upon tensile loading, the $\langle 1\,1\,0 \rangle/\{1\,1\,1\}$ wire first undergoes elastic deformation (O→A in Fig. 1) and all the input mechanical work is stored as strain energy (U_{110}) in the wire, i.e. $U_{110} = W$. Substitution of U_{110} into Eq. (12) yields the stress–strain relation

$$\sigma = \sigma_{110} = \frac{1}{V_0} \frac{\partial U_{110}}{\partial \varepsilon} = \frac{\partial u_{110}}{\partial \varepsilon}. \tag{15}$$

4.2. Dislocation nucleation at the initiation of lattice reorientation

The lattice reorientation begins when the $\langle 1\,1\,0 \rangle/\{1\,1\,1\}$ wire reaches its elastic limit at ε_s, as shown in Fig. 1. Beyond ε_s, a single dislocation is emitted and glides across the wire, forming a coherent twin boundary. Therefore, the initiation of the lattice reorientation is very similar to the initiation of plasticity because both processes involve defect nucleation.

The dislocation nucleation in nanowires is heterogeneous because wires have large free surface-to-volume ratios and sharp inter-facet edges due to the rhombic cross-sectional shape (Dumitrica et al., 2006). Various researchers have shown that the lowest energy barrier for the nucleation of dislocations corresponds to a path that initiates from the free surface with or without defects (Trushin et al., 2002). The four inter-facet edges are the most probable nucleation sites because atoms at these edges are the most underbonded. Consider now a $\{1\,1\,1\}$ slip plane, shown in Fig. 7. Vertices A and A′ are the likely nucleation sites for $\frac{1}{6}(1\,1\,1)[1\,1\,\bar{2}]$ Shockley partial dislocations because the long diagonal
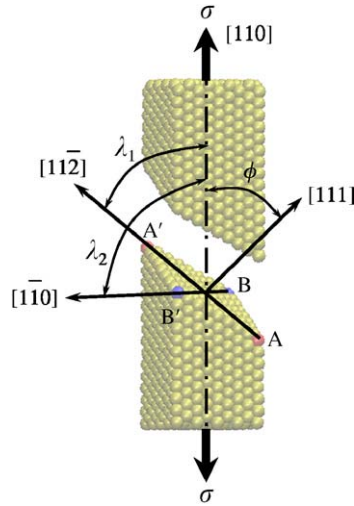
Fig. 7. Two separated portions of a wire showing a model to calculate the resolved shear stress, σ is the external loading stress, ϕ is the angle between the loading direction and the normal to the {1 1 1} slip plane, λ_1 is the angle between the loading direction and the [1 1 $\bar{2}$] slip direction for a Shockley partial dislocation, and λ_2 is the angle between the loading direction and the [1 $\bar{1}$ 0] slip direction for a full dislocation.

AA′ coincides with the [1 1 $\bar{2}$] slip direction. Similarly, vertices B and B′ are the likely nucleation sites for (1 1 1)[1 $\bar{1}$ 0] full dislocations because the short diagonal BB′ coincides with the [1 $\bar{1}$ 0] slip direction. Using the critical resolved shear stress (CRSS) criterion, we demonstrate that partial dislocation slip is more favorable than full dislocation slip. Specifically, we know that the RSS is given by

$$RSS = \sigma_1 \cos \phi \cos \lambda, \tag{16}$$

where σ_1 is the local stress at the nucleation sites and $\cos \phi \cos \lambda$ the Schmid factor. The Schmid factor for (1 1 1)[1 $\bar{1}$ 0] slip system is zero because the loading direction [1 1 0] is perpendicular to the slip direction [1 $\bar{1}$ 0], i.e. $\lambda = 90°$, as shown in Fig. 7. This makes the activation of (1 1 1)[1 $\bar{1}$ 0] slip systems highly unlikely. At the same time, the Schmid factor for (1 1 1)[1 1 $\bar{2}$] is 0.43 with $\phi = 35.3°$ and $\lambda = 53°$. Consequently, (1 1 1)[1 1 $\bar{2}$] is more favored for nucleation and slip, leading to a twinning deformation mechanism.

It is found that the yield stresses of nanowires decrease with increasing wire size. The same trend is also observed in gold nanowires (Gall et al., 2004). This size dependence is primarily due to the surface-stress-induced compressive stresses in the core of nanowires described in Section 3.2 (Diao et al. (2004b) and Gall et al. (2004)). Under tensile loading, the external stress needs to overcome the internal compressive stress first and then cause yielding of the wire. Since the magnitude of the internal compressive stresses increases with decreasing wire size, the overall yield stress decreases with increasing wire size.

In addition to the dependence on wire size, various researchers have shown that dislocation nucleation is also a kinetic process which depends on loading rate and temperature (Schuh et al., 2005). The rate effect can be neglected here because we only consider quasi-static processes. Suppose the nucleation of a dislocation requires an activation energy u_a, which is closely related to the unstable stacking fault energy. This energy barrier can be lowered through mechanical work, or be overcome by an appropriate

thermal fluctuation, or a combination of both. The probability of such an event in a given volume of material is written as (Schuh et al., 2005)

$$\dot{n} = \dot{n}_0 \cdot \exp\left(-\frac{u_a - \sigma V}{kT}\right), \tag{17}$$

where the attempt frequency for the event is $\dot{n}_0$ per unit volume, the mechanical work is the product of the stress σ and an activation volume V, and the thermal energy is the product of Boltzmann's constant k and temperature T. Since thermal fluctuations facilitate dislocation nucleation, less mechanical work is needed for dislocation nucleation at higher temperatures. Therefore, the yield stress is lower at higher temperatures, as shown in Fig. 8(b). The same trend is also observed in nanoindentation (Schuh et al., 2005).
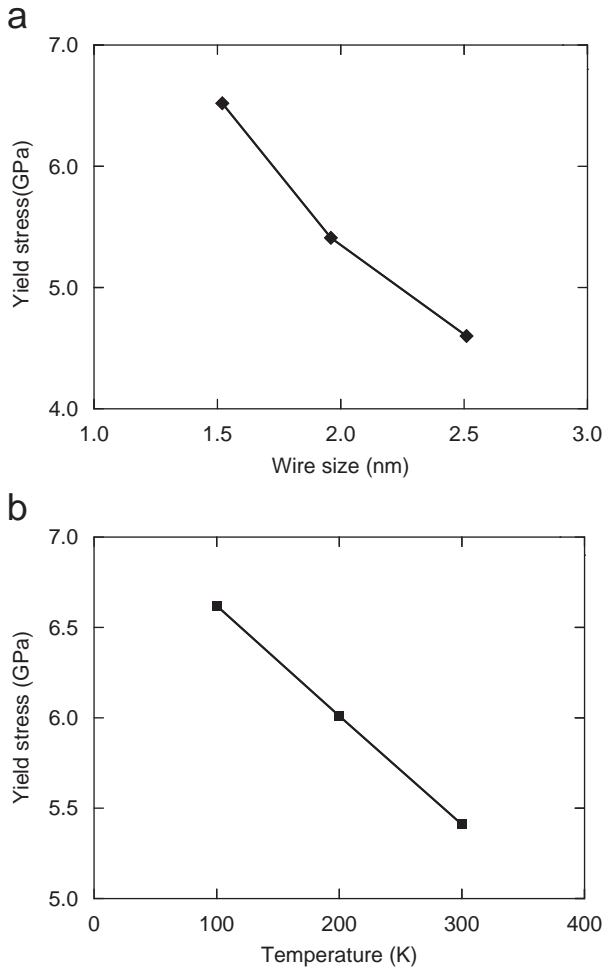

Fig. 8. Size and temperature dependence of the yield stress σ_y: (a) the variation of σ_y with wire size and (b) the variation of σ_y with temperature.

After partial dislocation nucleation, the stress drops precipitously because of the energy dissipation and stress relaxation associated with the dislocation propagation, as shown in Fig. 1. The partial dislocation moves along the {1 1 1} plane across the wire and leads to the formation of a twin. Subsequently, the wire enters a phase-equilibrium state at Point B, which will be discussed in the next section.

4.3. Lattice reorientation through twin boundary propagation

During lattice reorientation, the $\langle 1\,1\,0 \rangle/\{1\,1\,1\}$ and $\langle 0\,0\,1 \rangle/\{1\,0\,0\}$ phases coexist in the wire, separated by a coherent twin boundary. During the deformation, the $\langle 1\,1\,0 \rangle/\{1\,1\,1\}$ phase progressively transforms into the $\langle 0\,0\,1 \rangle/\{1\,0\,0\}$ phase as the twin boundary sweeps down the length of the wire. The lattice reorientation is a dissipative process even under isothermal, quasi-static deformation conditions. In this study, the lattice reorientation process is decomposed into two parts: a reversible part and an irreversible part. For the reversible part, we assume the wire *smoothly* goes through a series of phase-equilibrium states. Nonetheless, the actual transitions between equilibrium states are not smooth because there are barriers associated with lattice-scale defect nucleation (discussed later). Hence, twin boundary propagation produces a serrated strain energy landscape (see Fig. 1) with local peaks corresponding to unstable states and local minima corresponding to metastable states. The wire successively passes through unstable states and then settles into metastable states after overcoming the barrier. Meanwhile, the work required to overcome the barrier is released when the system settles into a metastable state. This release produces thermal energy, which is dissipated in the system by the constant temperature thermostat used in the present isothermal simulation. The first law of thermodynamics dictates that

$$W = \Delta U + Q, \tag{18}$$

where W is the total input work, Q the energy dissipation associated with the irreversible process. ΔU is the change in strain energy associated with the reversible process, i.e.,

$$\Delta U = U - U_0, \tag{19}$$

with U being the strain energy at the phase-equilibrium state during the deformation and U_0 being the strain energy of the unstressed $\langle 1\,1\,0 \rangle/\{1\,1\,1\}$ wire. Eqs. (12) and (18) combine to give

$$\sigma = \frac{1}{V_0}\left(\frac{\partial(\Delta U)}{\partial \varepsilon} + \frac{\partial Q}{\partial \varepsilon}\right) = \sigma_e + \sigma_{\text{dissip}}, \tag{20}$$

where σ_e is the part of the stress needed to drive the transition of the phase-equilibrium states. It is determined by the elastic properties of the two phases. Specifically,

$$\sigma_e = \frac{1}{V_0}\frac{\partial(\Delta U)}{\partial \varepsilon} = \frac{1}{V_0}\frac{\partial(U - U_0)}{\partial \varepsilon} = \frac{1}{V_0}\frac{\partial U}{\partial \varepsilon}. \tag{21}$$

σ_{dissip} is the part of the stress required to drive or absorb the nucleation, propagation, and annihilation of partial dislocations associated with the twin boundary propagation. Obviously,

$$\sigma_{\text{dissip}} = \frac{1}{V_0}\frac{\partial Q}{\partial \varepsilon}. \tag{22}$$

In the following discussion, the reversible and irreversible parts of the lattice reorientation process will be analyzed individually. First, the governing equation for a single phase-equilibrium state will be derived based on the constrained minimization of strain energies. The reversible smooth transition is obtained by solving these governing equations for a series of phase-equilibrium states. Second, the source and mechanism of the energy dissipation part are analyzed through the perspective of lattice-scale dislocation activities and the characteristics of the associated energy landscape. This analysis allows the dissipative process to be quantified.

4.3.1. Non-dissipative smooth transition between phase-equilibrium states

1. *Kinematics*

Consider a phase-equilibrium state corresponding to a nominal strain ε in which two phases coexist and are separated by a twin boundary, as shown in Fig. 3. Each phase is elastically stretched. Therefore, the following field equations are satisfied:

$$\varepsilon_i = \frac{\mathrm{d}\delta_i}{\mathrm{d}x} \text{ in each phase} \tag{23}$$

and

$$\delta^+ = \delta^- \text{ at the twin boundary.} \tag{24}$$

Here, δ_i is the axial displacement of the wire. For the $\langle 1\,1\,0 \rangle/\{1\,1\,1\}$ phase, $i = 1\,1\,0$ and $\delta_i = \delta_{110}$; for the $\langle 0\,0\,1 \rangle/\{1\,0\,0\}$ phase, $i = 0\,0\,1$ and $\delta_i = \delta_{001}$. Similarly, ε_i is the local strain in the wire with $\varepsilon_i = \varepsilon_{110}$ in the $\langle 1\,1\,0 \rangle/\{1\,1\,1\}$ phase and $\varepsilon_i = \varepsilon_{001}$ in the $\langle 0\,0\,1 \rangle/\{1\,0\,0\}$ phase. δ^+ and δ^- denote the limiting values of the displacement on the two sides of the twin boundary. Eqs. (23) and (24) imply that the displacement is continuous within each phase and across the twin boundary, but the elastic strains are not necessarily the same in the two phases. Generally, there is a strain jump across the twin boundary.

It is important to note that the total strain ε includes not only contributions from the elastic strains in two phases (ε_{110} and ε_{001}), but also the transformation strain ($\varepsilon_{\mathrm{tr}}$) due to the phase transformation. Specifically,

$$\varepsilon = \frac{l - l_0}{l_0} \tag{25}$$

and

$$l = l_{110} + l_{001}. \tag{26}$$

Here, l_0 is the initial total length of the stress-free $\langle 1\,1\,0 \rangle/\{1\,1\,1\}$ wire, l the current length of the wire, and l_{110} and l_{001} are, respectively, the current lengths of the $\langle 1\,1\,0 \rangle/\{1\,1\,1\}$ and $\langle 0\,0\,1 \rangle/\{1\,0\,0\}$ phases corresponding to the total nominal strain ε. Note that

$$l_{110} = l_{110}^0(1 + \varepsilon_{110}) \tag{27}$$

and

$$l_{001} = l_{001}^0(1 + \varepsilon_{001}), \tag{28}$$

where l_{110}^0 and l_{001}^0 are the lengths of the $\langle 1\,1\,0 \rangle/\{1\,1\,1\}$ and $\langle 0\,0\,1 \rangle/\{1\,0\,0\}$ phases in their unstressed states, respectively. Another kinematic condition that must be satisfied

during lattice reorientation is that the sum of the lengths of the untransformed $\langle 1\,1\,0 \rangle /$
$\{1\,1\,1\}$ phase and the transformed $\langle 1\,1\,0 \rangle / \{1\,1\,1\}$ phase must equal the total length of
the initial undeformed wire, i.e.,

$$l_{110}^0 + \frac{l_{001}^0}{1 + \varepsilon_{\mathrm{tr}}} = l_0. \tag{29}$$

Here, $l_{001}^0/(1 + \varepsilon_{\mathrm{tr}})$ is the length of the transformed $\langle 1\,1\,0 \rangle / \{1\,1\,1\}$ phase as calculated
from the length of the corresponding $\langle 0\,0\,1 \rangle / \{1\,0\,0\}$ phase.

2. *Force balance*

In addition to the above kinematics equations, the stress field in each phase must satisfy
the force balance condition. Specifically,

$$\frac{\mathrm{d}\sigma_i}{\mathrm{d}x} = 0 \text{ in each phase} \tag{30}$$

and

$$\sigma_{110} A_{110} = \sigma_{001} A_{001} \text{ at the phase boundary.} \tag{31}$$

Here, σ_i is the axial stress in the wire. For the $\langle 1\,1\,0 \rangle / \{1\,1\,1\}$ phase, $\sigma_i = \sigma_{110}$; for the
$\langle 0\,0\,1 \rangle / \{1\,0\,0\}$ phase, $\sigma_i = \sigma_{001}$. A_{110} is the area of the rhombic cross-section of the
$\langle 1\,1\,0 \rangle / \{1\,1\,1\}$ phase, and A_{001} is the area of the square cross-section of the $\langle 0\,0\,1 \rangle /$
$\{1\,0\,0\}$ phase. Eqs. (30) and (31) imply that the force is continuous within each phase
and across the twin boundary, and the stress is uniform within each phase but not
continuous across the twin boundary because the cross-sectional areas of the two phases
are not the same. Specifically, $A_{110} > A_{001}$.

3. *Constrained minimization of strain energies*

A system in its equilibrium state has the minimum strain energy. Therefore, we can
obtain the phase-equilibrium state of the wire by minimizing the total strain energy
subject to the force balance and kinematics constraints. The total strain energy of the
wire is composed of the strain energy of each phase and the interface energy, i.e.,

$$U = \int_{V_{110}} u_{110}(\varepsilon_{110})\,\mathrm{d}V + \int_{V_{100}} u_{001}(\varepsilon_{001})\,\mathrm{d}V + U_{\mathrm{interface}}. \tag{32}$$

Note that the strain energy associated with the twin boundary is essentially constant
because the configuration of the coherent twin boundary remains the same during
lattice reorientation. Therefore, the twin boundary energy does not affect the
minimization of the strain energy (until it disappears).

The constrained energy minimization problem can be illustrated by a common tangent
construction between the strain energy density functions of the $\langle 1\,1\,0 \rangle / \{1\,1\,1\}$ and
$\langle 0\,0\,1 \rangle / \{1\,0\,0\}$ phases in Fig. 9. Points M and N share a comment tangent and, hence,
are in the same stress state because the tangents of strain energy density functions give
the stresses at the corresponding tangent points. Therefore, points M and N have
minimum strain energies subject to the force balance constraints. Consequently,
these two tangent points represent the phase-equilibrium states in a binary phase
system. Note that in order to compare the forces in the two phases, the strain energy
density function of the $\langle 0\,0\,1 \rangle / \{1\,0\,0\}$ phase is normalized by the ratio between the
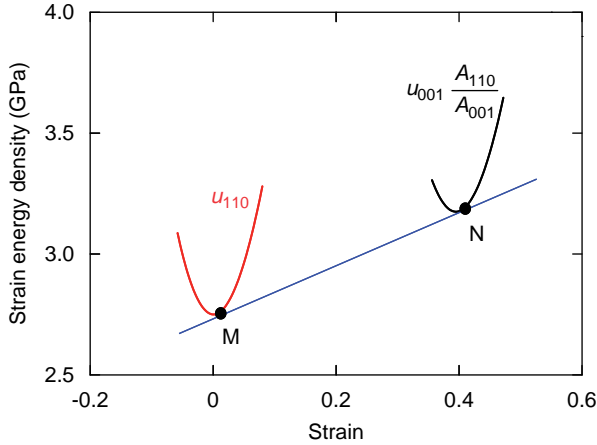
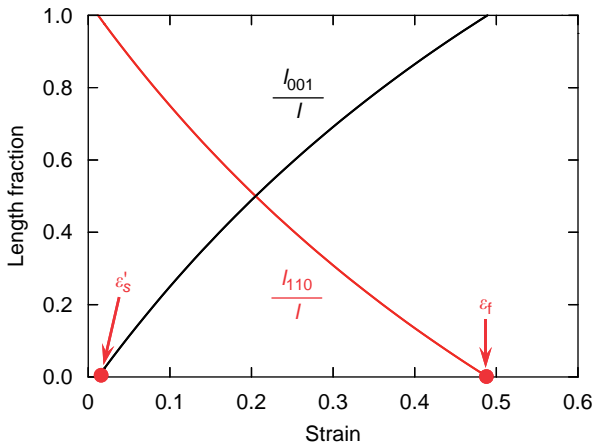Fig. 9. Phase-equilibrium illustrated by a common tangent construction.

Fig. 10. The variation of length fractions of the $\langle 1\,1\,0 \rangle/\{1\,1\,1\}$ and $\langle 0\,0\,1 \rangle/\{1\,0\,0\}$ phases during lattice reorientation.

cross-sectional areas (A_{110}/A_{001}) to account for the difference in the cross-sectional areas, see Eq. (31).

Eqs. (23)–(32) are the governing equations for a phase-equilibrium state at a given strain ε. Solving these equations numerically yields the elastic stresses (σ_{110} and σ_{001}), strains (ε_{110} and ε_{001}), and the length fractions (l_{110}/l and l_{001}/l) in the two phases at the given strain ε. This solution process is repeated for strains from 0 to 0.6 with a stain increment of 0.01 to obtain the stress and strain states and the length fractions throughout the transformation process. It is found that the stresses and strains of the two phases are constant during the lattice reorientation. This can also be seen from the common tangent construction in Fig. 9. Therefore, the elongation during lattice reorientation proceeds solely through variations in the length fractions of the two phases, as shown in

Fig. 10. The length fractions also clearly depict the three deformation stages:

(1) The initial elastic deformation of the single-phase $\langle 1\,1\,0 \rangle/\{1\,1\,1\}$ wire $(0 \sim \varepsilon_s)$ corresponds to $l_{110}/l = 1$ and $l_{001}/l = 0$. Note that the actual elastic limit is ε_s, not ε_s' (see Fig. 1). While ε_s at the yield point corresponds to an unstable state, ε_s' corresponds to a phase-equilibrium state predicted by the preceding governing equations. Although the condition for phase-equilibrium states is first reached at ε_s', phase transformation does not immediately start because of the energy barrier for dislocation nucleation (discussed later in Section 4.2). The actual phase transformation begins at ε_s when the stored strain energy is sufficient to overcome the energy barrier for dislocation nucleation.

(2) The lattice reorientation proceeds under loading $(\varepsilon_s \sim \varepsilon_f)$ through the decrease of l_{110}/l and increase of l_{001}/l. The total nominal strain at the completion of the reorientation process (ε_f) corresponds to the state when l_{110}/l is reduced to zero (point C in Fig. 1).

(3) The elastic deformation of the single-phase $\langle 0\,0\,1 \rangle/\{1\,0\,0\}$ wire $(\varepsilon_f \sim)$ corresponds to $l_{110}/l = 0$ and $l_{001}/l = 1$.

4. *Elastic stress component σ_e*

With the local stresses obtained from the constrained minimization of strain energies, the stress component σ_e can be derived from Eq. (21). Specifically, substitution of Eq. (32) into Eq. (21) yields the elastic stress component σ_e as

$$
\begin{aligned}
\sigma_e &= \frac{1}{V_0}\frac{\partial U}{\partial \varepsilon} = \frac{1}{V_0}\frac{\partial}{\partial \varepsilon}(V_{110}u_{110} + V_{001}u_{001} + U_{\text{interface}}), \\
&= \frac{1}{V_0}\left(V_{110}\frac{du_{110}}{d\varepsilon_{110}}\frac{\partial \varepsilon_{110}}{\partial \varepsilon} + V_{100}\frac{du_{001}}{d\varepsilon_{001}}\frac{\partial \varepsilon_{001}}{\partial \varepsilon}\right), \\
&= \left(\frac{V_{110}}{V_0}\frac{\partial \varepsilon_{110}}{\partial \varepsilon}\right)\sigma_{110} + \left(\frac{V_{001}}{V_0}\frac{\partial \varepsilon_{001}}{\partial \varepsilon}\right)\sigma_{001}.
\end{aligned}
\tag{33}
$$

Here, $V_0 = A_{110}l_0$ is the initial total volume of the wire, $V_{110} = A_{110}l_{110}^0$ and $V_{001} = A_{001}l_{001}^0$ are the volumes of the $\langle 1\,1\,0 \rangle/\{1\,1\,1\}$ and $\langle 0\,0\,1 \rangle/\{1\,0\,0\}$ phases in the unstressed states, respectively. In order to calculate $\partial\varepsilon_{110}/\partial\varepsilon$ and $\partial\varepsilon_{001}/\partial\varepsilon$, we consider an infinitesimal deformation of $d\varepsilon$. The total deformation increment is equal to the sum of the deformation increments of the two phases (Eqs. (25)–(28)), i.e.,

$$
(l_{110}^0 + l_{001}^0)\,d\varepsilon = l_{110}^0\,d\varepsilon_{110} + l_{001}^0\,d\varepsilon_{001}.
\tag{34}
$$

Also, the two phases must satisfy the force balance condition in Eq. (31), which can be rewritten as

$$
\frac{d\sigma_{110}}{d\varepsilon_{110}}d\varepsilon_{110}A_{110} = \frac{d\sigma_{001}}{d\varepsilon_{001}}d\varepsilon_{001}A_{001}.
\tag{35}
$$

Equations (33), (34), and (35) combine to give

$$
\sigma_e = \lambda_{110}\sigma_{110} + \lambda_{001}\sigma_{001},
\tag{36}
$$

where

$$\lambda_{110} = \frac{l_{110}^0}{l_0} \frac{l_{110}^0 + l_{001}^0}{l_{110}^0 + \left(\frac{A_{110}}{A_{001}}\right)\left(\frac{\mathrm{d}\sigma_{110}}{\mathrm{d}\varepsilon_{110}} \middle/ \frac{\mathrm{d}\sigma_{001}}{\mathrm{d}\varepsilon_{001}}\right) l_{001}^0} \tag{37}$$

and

$$\lambda_{001} = \frac{l_{001}^0}{l_0} \frac{l_{110}^0 + l_{001}^0}{\left(\frac{\mathrm{d}\sigma_{100}}{\mathrm{d}\varepsilon_{100}} \middle/ \frac{\mathrm{d}\sigma_{110}}{\mathrm{d}\varepsilon_{110}}\right) l_{110}^0 + \left(\frac{A_{110}}{A_{100}}\right) l_{001}^0} . \tag{38}$$

At the initiation of the lattice reorientation,

$$l_{110}^0 = l_0 \text{ and } l_{001}^0 = 0. \tag{39}$$

Through Eqs. (37) and (38), the above statement implies

$$\lambda_{110} = 1 \text{ and } \lambda_{001} = 0. \tag{40}$$

Therefore,

$$\sigma_e = \sigma_{110}. \tag{41}$$

Similarly, at the completion of the lattice reorientation,

$$l_{110}^0 = 0 \text{ and } l_{001}^0 = l_0(1 + \varepsilon_{tr}). \tag{42}$$

Through Eqs. (37) and (38), this implies

$$\lambda_{110} = 0 \text{ and } \lambda_{001} = (1 + \varepsilon_{tr})(A_{001}/A_{110}). \tag{43}$$

Therefore,

$$\sigma_f = (1 + \varepsilon_{tr})(A_{001}/A_{110})\sigma_{001}. \tag{44}$$

From Eq. (31), it can be seen that $\sigma_{110} < \sigma_{001}$ because $A_{110} > A_{001}$. Therefore, σ_e is at a minimum value of $\sigma_e = \sigma_{110}$ at the initiation of lattice reorientation and a maximum value of $\sigma_e = (1 + \varepsilon_{tr})(A_{001}/A_{110})\sigma_{001}$ at the completion of lattice reorientation. Between these two states, σ_e increases as the low stress $\langle 1\,1\,0 \rangle$ phase gradually transforms into the high-stress $\langle 0\,0\,1 \rangle$ phase. As will be discussed in the next subsection, the stress component σ_{dissip} is constant during the reorientation. Therefore, this increase of σ_e is the primary reason behind the increase of $\sigma = \sigma_e + \sigma_{dissip}$ over the same stage of deformation.

4.3.2. Dissipative twin boundary propagation

The smooth transition between phase-equilibrium states discussed in the preceding subsection is an ideal process, which is thermodynamically reversible without energy dissipation. Nonetheless, the actual lattice reorientation is a dissipative process, no matter
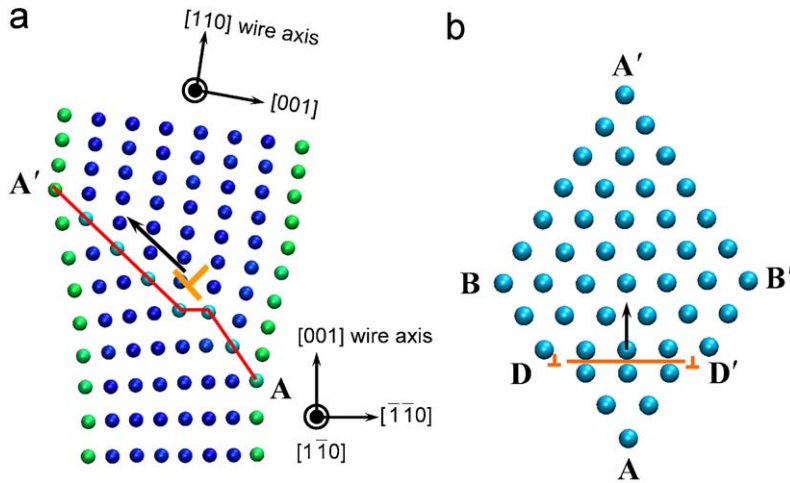
Fig. 11. Twin boundary propagation through dislocation nucleation, glide, and annihilation: (a) a side view of details of the $\{1\,1\,1\}$ twin boundary and the $\frac{1}{6}\{1\,1\,1\}\langle 1\,1\,2\rangle$ Shockley partial dislocation and (b) a perpendicular view of the same $\{1\,1\,1\}$ twin boundary and the gliding partial dislocation.

how slow the transformation occurs. The energy dissipation is due to the ruggedness of the energy landscape associated with the lattice reorientation. This ruggedness is due to the propagation of lattice-scale defects (Vainchtein and Rosakis, 1999; Puglisi and Truskinovsky, 2002; Truskinovsky and Vainchtein, 2003, 2004). Therefore, it is important to study the detailed lattice-scale transformation mechanism during the twin boundary propagation and the associated energy landscape.

The twin boundary propagates along the wire axis because the atoms on one side of the twin boundary undergo a shear deformation relative to atoms on the other side. However, atoms on one side do not shear simultaneous because the energy barrier for such a uniform motion is too high. Instead, the shear deformation proceeds through sequential nucleation, glide, and annihilation of $\frac{1}{6}\langle 1\,1\,2\rangle$ Shockley partial dislocations (Abeyaratne and Vedantam, 2003), as shown in Fig. 11. Due to the energy barriers for dislocation nucleation and migration, the strain energy function has a serrated shape with local peaks (u_i') corresponding to unstable states and local minima (u_i) corresponding to metastable states. The wire is periodically brought to unstable states and then settles into the metastable states after overcoming the barrier. Specifically, consider a phase-equilibrium state corresponding to local minimum at Point u_1 in Fig. 12(a). At this state, the twin boundary is an atomically smooth $\{1\,1\,1\}$ plane. The twin boundary propagates in a "stick–slip" manner described below (Vainchtein and Rosakis, 1999):

(1) *Elastic stretching*: the strain energy increases along curve $u_1 u_2'$ as the wire is stretched.
(2) *Dislocation nucleation*: the wire becomes unstable when the strain energy increases to the local energy peak at point u_2'. A partial dislocation is then nucleated from one sharp edge (point A in Fig. 11) on the atomic plane adjacent to the twin plane. The atoms at the nucleation site have lower coordination numbers and thus constitute a weak spot for dislocation nucleation.
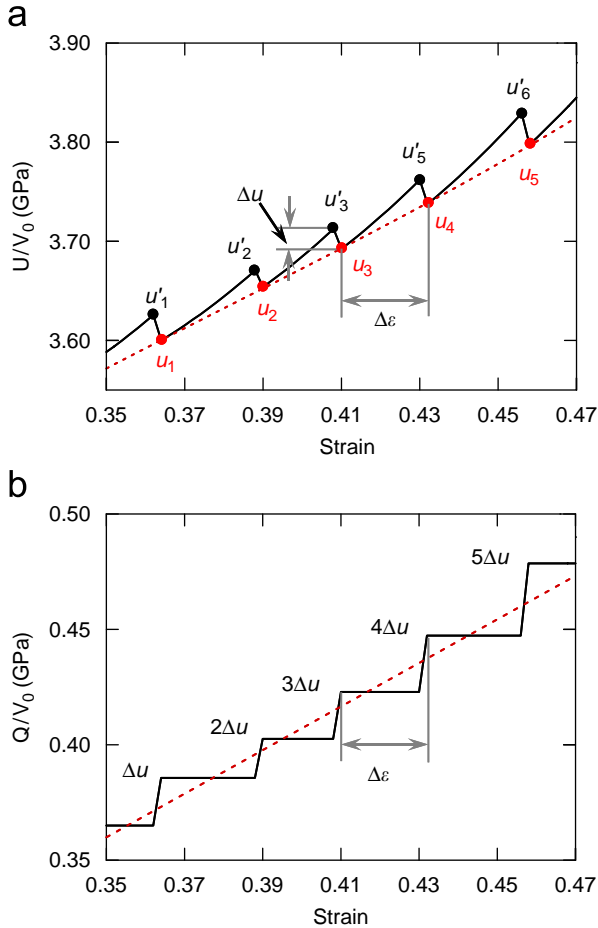
Fig. 12. (a) The serrated strain energy curve during lattice reorientation, the local peaks correspond to the instability upon nucleation of partial dislocation, and the local minima correspond to phase-equilibrium states and (b) the stepwise energy dissipation curve.

(3) *Dislocation glide*: after the dislocation is nucleated, the dislocation line (DD′ in Fig. 11) forms a step on the twin boundary. Hence, the twin boundary is not atomically smooth any more. The dislocation step line glides along the long diagonal from point A to A′. Meanwhile, the lattice is relaxed and the strain energy drops precipitously along strain energy curve u'_2u_2. A more careful analysis would show that the path u'_2u_2 is also serrated since dislocation glide itself is almost always thermally activated.

(4) *Dislocation annihilation*: the partial dislocation annihilates when it reaches the far edge of the sample (indicated by A′ in Fig. 11).

Steps (1)–(4) above correspond to the translation of the twin boundary by a single interplanar distance, leaving the twin boundary atomically smooth again. Meanwhile, the wire reaches another metastable phase-equilibrium state with local strain energy minimum

at point u_2. As the wire is further stretched, the process described in Steps (1)–(4) repeats. In each cycle, the wire is brought to an unstable state through elastic stretching and then settles in a local metastable phase-equilibrium state through dislocation nucleation, gliding, and annihilation. At the same time, the twin boundary advances by an inter-planar distance between two neighboring $\{1\,1\,1\}$ planes. Consequently, the strain energy curve exhibits a serrated shape with local minima u_i corresponding to metastable states and local maxima u_i' corresponding to unstable states. It is important to note that the dotted line in Fig. 12(a) illustrates the reversible, smooth transition path between metastable states governed by the equations in Section 4.3.1. On the other hand, the serrated strain energy density curve shows the actual change of strain energy density during the deformation. Each time a dislocation is nucleated and glides across the wire, the strain energy drops precipitously from the local maximum u_i' to minimum u_i. At the same time, the strain energy difference $\Delta u = u_i' - u_i$ is dissipated as heat (phonons), which is transferred to the thermal reservoir that maintains the specimen at a constant temperature. During the elastic stretching described in Step (1), all input energy is stored as strain energy in the wire and there is no energy dissipation. Therefore, the energy dissipation shows a stepwise increase with strain, as shown in Fig. 12(b). Without thermal fluctuations, Δu is essentially constant because the energy barriers for dislocation nucleation are the same throughout the lattice orientation process. Therefore, the total energy dissipation is

$$Q = V_0 n \Delta u, \tag{45}$$

where n is the number of cycles of the dislocation activities described in Steps (1)–(4). The stepwise change of Q can also be approximated by the straight line (the dotted line in Fig. 12(b)):

$$Q = V_0 \frac{n - 0.5}{n} \frac{\Delta u}{\Delta \varepsilon} \varepsilon \approx V_0 \frac{\Delta u}{\Delta \varepsilon} \varepsilon, \tag{46}$$

where $\Delta \varepsilon$ is the strain increment corresponding to one cycle of dislocation nucleation and annihilation described in Steps (1)–(4). It is essentially constant. Substitution of Eq. (46) into (22) yields

$$\sigma_{\text{dissip}} = \frac{\Delta u}{\Delta \varepsilon}. \tag{47}$$

σ_{dissip} as quantified here is an average measure which is constant throughout the reorientation process because both Δu and $\Delta \varepsilon$ are essentially constant. Moreover, σ_{dissip} is proportional to Δu, which is closely related to the energy barrier for dislocation nucleation, similar to what was described in Section 4.2. The difference is that the dislocation nucleation discussed in Section 4.2 is associated with the *formation* of a twin boundary and is nucleated from a perfect crystal without initial defects. In contrast, the dislocation nucleation here is associated with the *propagation* of the twin boundary and is nucleated nearly at the existing twin boundary. Therefore, the latter has a lower-energy barrier, but both processes have similar temperature effects. Eq. (17) suggests that less mechanical work is necessary for dislocation nucleation at higher temperatures because thermal fluctuations facilitate overcoming the energy barrier. Therefore, Δu and σ_{dissip} are smaller at higher temperatures, as shown in Fig. 13. This indicates that less mechanical work is necessary to move the twin boundary as the temperature increases.
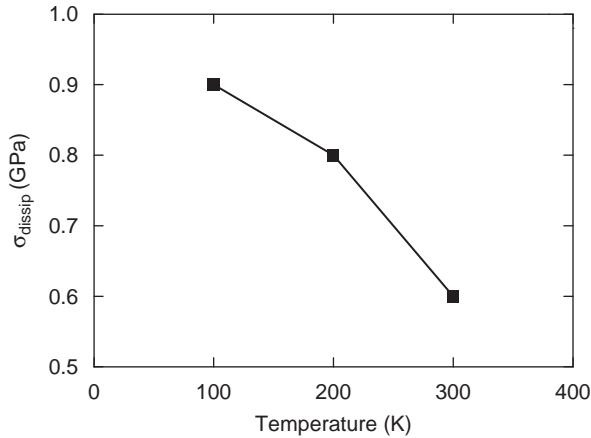
Fig. 13. The variation of σ_{dissip} with temperature of a $1.96 \times 1.96\,\text{nm}$ $\langle 1\,1\,0 \rangle / \{1\,1\,1\}$ Cu wire.

4.4. Elastic deformation of the $\langle 0\,0\,1 \rangle / \{1\,0\,0\}$ phase

At the completion of the lattice reorientation, the wire is transformed into a single $\langle 0\,0\,1 \rangle / \{1\,0\,0\}$ phase. The subsequent deformation is purely elastic and no energy dissipation occurs. Therefore, all of the input mechanical work is stored in the wire as strain energy, i.e.,

$$W = U_{001}. \tag{48}$$

Eqs. (12) and (48) specify the stress–strain relation for this stage as

$$\sigma = \frac{1}{V_0} \frac{\partial U_{001}}{\partial \varepsilon_{001}} = \frac{\partial u_{001}}{\partial \varepsilon_{001}}, \tag{49}$$

where u_{100} is the strain energy density of the single-phase $\langle 0\,0\,1 \rangle / \{1\,0\,0\}$ wires in Fig. 6 and ε_{100} is the strain measured relative to the unstressed state of the $\langle 0\,0\,1 \rangle / \{1\,0\,0\}$ phase. As previously mentioned, the reference state for nominal strain ε is the unstressed state of the $\langle 1\,1\,0 \rangle / \{1\,1\,1\}$ phase. We know that, if the length of the unstressed $\langle 1\,1\,0 \rangle / \{1\,1\,1\}$ phase is l_{110}^0, the length of the corresponding $\langle 0\,0\,1 \rangle / \{1\,0\,0\}$ phase is $l_{110}^0(1 + \varepsilon_{\text{tr}})$. Hence, since $\varepsilon = \varepsilon_{\text{f}}$ at the beginning of the elastic deformation of the $\langle 0\,0\,1 \rangle / \{1\,0\,0\}$ wire, the relation between ε and ε_{001} is

$$\varepsilon = \varepsilon_{\text{f}} + \varepsilon_{001}(1 + \varepsilon_{\text{tr}}). \tag{50}$$

The present analysis provides a prediction for the stress–strain relation of the initially $\langle 1\,1\,0 \rangle / \{1\,1\,1\}$ nanowire, including all three deformation stages (pure elastic deformation of the $\langle 1\,1\,0 \rangle / \{1\,1\,1\}$ and $\langle 0\,0\,1 \rangle / \{1\,0\,0\}$ phases and the lattice reorientation). Putting these together, we obtain a complete piecewise smooth model for the stress–strain behavior of metal nanowires under the conditions of isothermal quasi-static tensile deformation.

5. Comparison to MD simulations

5.1. MD simulation methods

In order to verify the model derived above, we performed a series of MD simulations to obtain the stress–strain behavior of Cu nanowires under the conditions of isothermal quasi-static tensile deformation. An embedded-atom-method (EAM) interatomic potential for Cu (Mishin et al., 1999, 2001) is used. Uniaxial displacement-controlled tensile loading are applied under simulated quasi-static conditions (Gall et al., 2004). Specifically, in each load step, all of the atoms are first displaced according to a prescribed uniform engineering strain increment of 0.125% in the length direction. The wires are then equilibrated with their ends fixed at constant temperature for 15 picoseconds (ps) to obtain a macroscopic equilibrium configuration at the prescribed strain. This relaxation process allows structural changes to occur, if the conditions so dictate. This process usually takes less than 12 ps and the average stress over the last 3 ps of the relaxation period at each load step is taken as the stress in the wire at the current strain. The wire is stretched till fracture occurs.

The preceding continuum model requires the strain energy density functions for the pure $\langle 1\,1\,0\rangle/\{1\,1\,1\}$ and $\langle 0\,0\,1\rangle/\{1\,0\,0\}$ phases as inputs. These strain energy functions can be obtained by either MD simulations or the analytical methods described in Section 3.2, provided that the bulk elastic constants and surface stresses are known. Here, the strain energy density functions are obtained by performing elastic deformations of the materials using MD simulations. Specifically, two unit cells are created out of perfect bulk lattice with the same cross-sections as the corresponding phases in a wire of interest. Periodic boundary conditions are applied in the axial directions. First, the unit cells are relaxed under zero traction (x and y directions) and zero stress (z direction) conditions. Due to the tensile surface stress, the unit cells contract in the axial direction and reach self-equilibrium states, as discussed in Section 3.2. Subsequently, the previously described displacement-controlled tensile loading is applied to the unit cells until yielding occurs. Suppose there are n atoms in a unit cell and the total internal energy of the unit cell obtained from MD simulations is U_i at a given temperature and suppose the total energy per atom in the bulk is u_{b} at the same temperature, the total strain energy of the unit cell is

$$U = U_i - nu_{\mathrm{b}}. \tag{51}$$

Application of Eq. (51) at each step allows the strain energy functions for the $\langle 1\,1\,0\rangle/\{1\,1\,1\}$ and $\langle 0\,0\,1\rangle/\{1\,0\,0\}$ pure phases within the elastic regime to be obtained.

These strain energy functions are used in the continuum model described in Section 4. The model predictions are compared with the results of MD simulations for wires of different sizes at different temperatures. The model predictions show excellent agreement with the results of MD simulations. They not only capture the major characteristics of the unique behavior due to lattice reorientation, but also account for the effects of size and temperature on the behavior.

5.2. Temperature effect

The elastic behaviors of single-phase wires are nearly independent of temperatures (the elastic constants are weakly temperature-dependent). As shown in Fig. 14, the strain energy density functions and stress–strain curves essentially coincide with each other
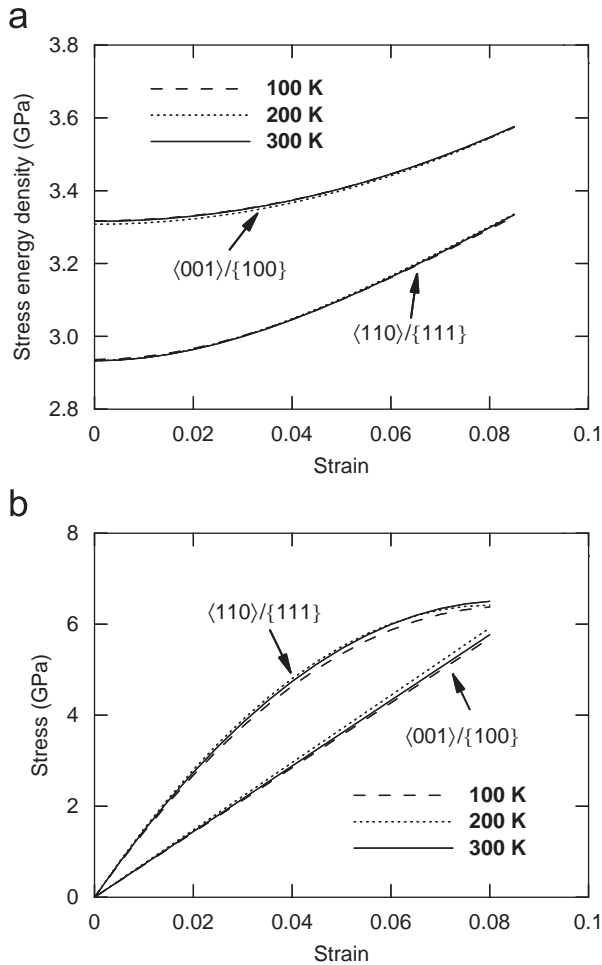
Fig. 14. The elastic behaviors of a single-phase 1.96×1.96 nm $\langle 1\,1\,0 \rangle/\{1\,1\,1\}$ Cu wire and the corresponding $\langle 0\,0\,1 \rangle/\{1\,0\,0\}$ wire at temperatures of 100, 200, and 300 K: (a) the strain energy density functions and (b) the stress–strain curves.

within the temperature range considered (100–300 K). However, the results of MD simulation show that lattice reorientation is temperature-dependent. Specifically, both the yield stress σ_y and the stress during lattice reorientation process decrease as temperature increases. This temperature effect can be explained by the model.

Consider the two components of the stress during transformation σ_e (associated with the phase-equilibrium states) and σ_{dissip} (associated with energy dissipation). Since σ_e is primarily determined by the elastic behavior of the two pure phases (Section 4.3.1), it is essentially independent of temperature (see Table 1) because the elastic behaviors of the pure phases are nearly temperature-independent over the temperature range examined here.

The effect of temperature on the wires' transformation behavior primarily comes from the temperature dependence of σ_{dissip}. Specifically, σ_{dissip} is lower at higher temperatures

Table 1
Continuum model parameters for a 1.96×1.96 nm Cu nanowire at different temperatures

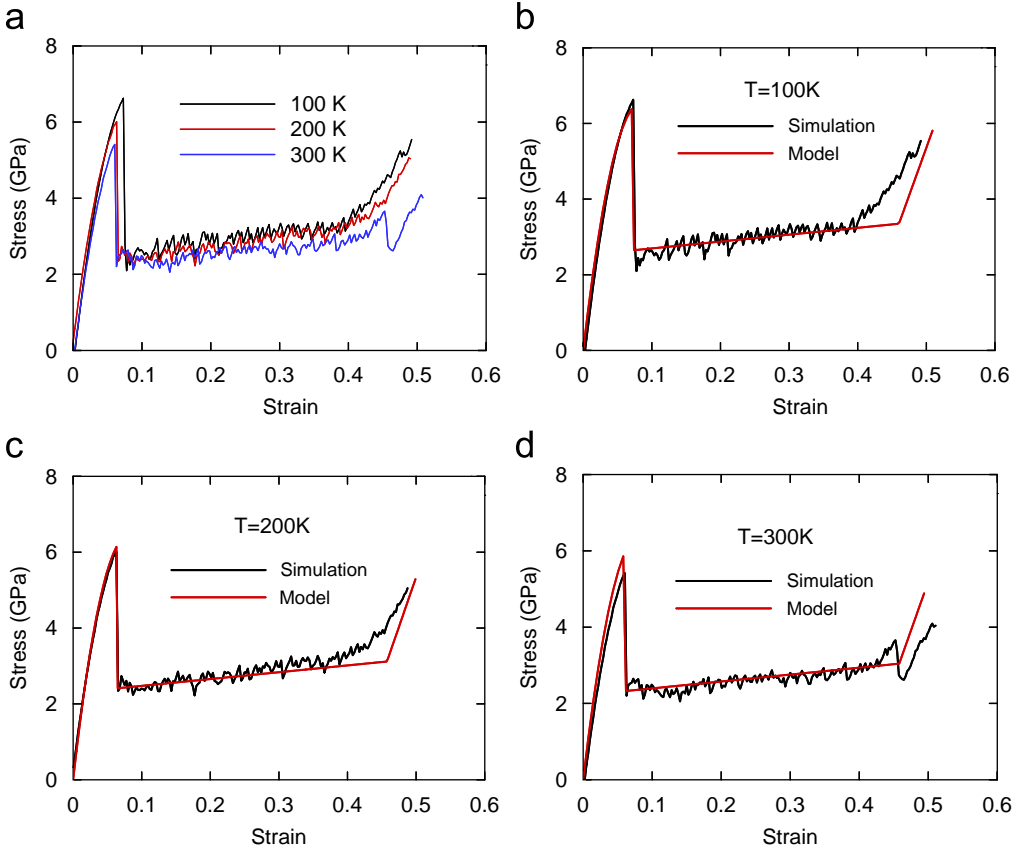| Temperature (K)	ε_s	σ_y (GPa)	ε_{110}	σ_{110} (GPa)	ε_f	ε_{100}	σ_{100} (GPa)	σ_{dissip} (GPa)
100	0.073	6.62	0.0119	1.82	0.46	0.0322	2.29	0.9
200	0.061	6.01	0.0112	1.80	0.457	0.0306	2.26	0.8
300	0.059	5.41	0.0116	1.81	0.459	0.0317	2.29	0.6

Fig. 15. Temperature effects: (a) the stress–strain behaviors of a 1.96×1.96 nm $\langle 110 \rangle/\{111\}$ Cu wire at temperatures of 100, 200, and 300 K obtained from MD simulations, figures (b)–(d) show the comparisons of the results of MD simulations with the model predictions at $T = 100$, 200, and 300 K, respectively.

because thermal fluctuations facilitate overcoming the energy barrier for dislocation nucleation. For the same reason, the yield stress is lower at higher temperatures. As shown in Fig. 15, the model accurately predicts the behavior of a $\langle 110 \rangle/\{111\}$ Cu nanowire with a lateral size of 1.96×1.96 nm over the entire range of temperature considered.

5.3. Size effects

Due to the higher surface-to-volume ratios, smaller wires have higher strain energy densities in the self-equilibrated states, as shown in Fig. 16(a). For the same reason, smaller wires are stiffer than larger wires, which can be seen from the stress–strain relations in
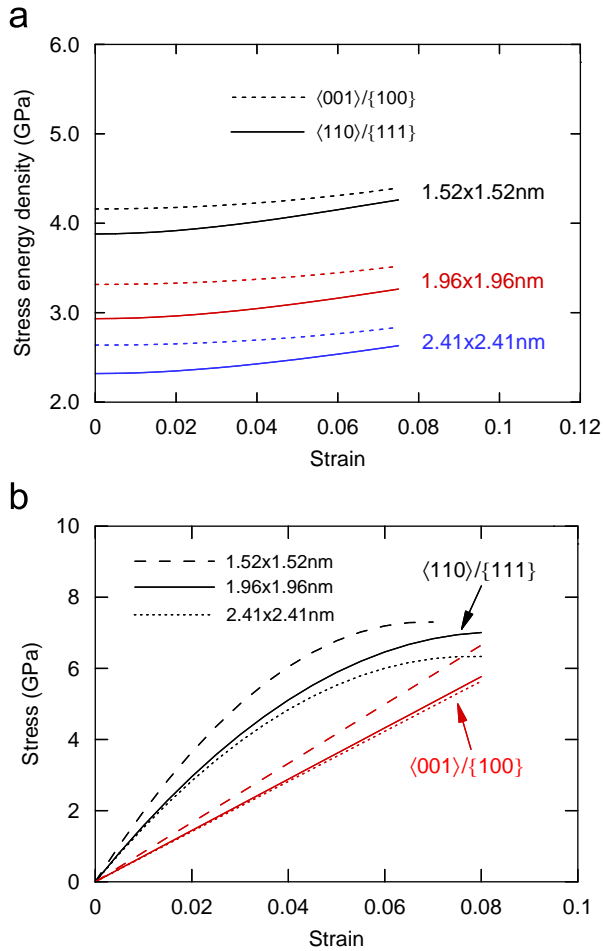

Fig. 16. The elastic behaviors of single-phase $\langle 1\,1\,0 \rangle / \{1\,1\,1\}$ and $\langle 0\,0\,1 \rangle / \{1\,0\,0\}$ Cu wires of different sizes at $T = 300\,\mathrm{K}$: (a) the strain energy density functions and (b) the stress–strain curves.

Table 2
Continuum model parameters for Cu wires of different sizes at $T = 300\,\mathrm{K}$

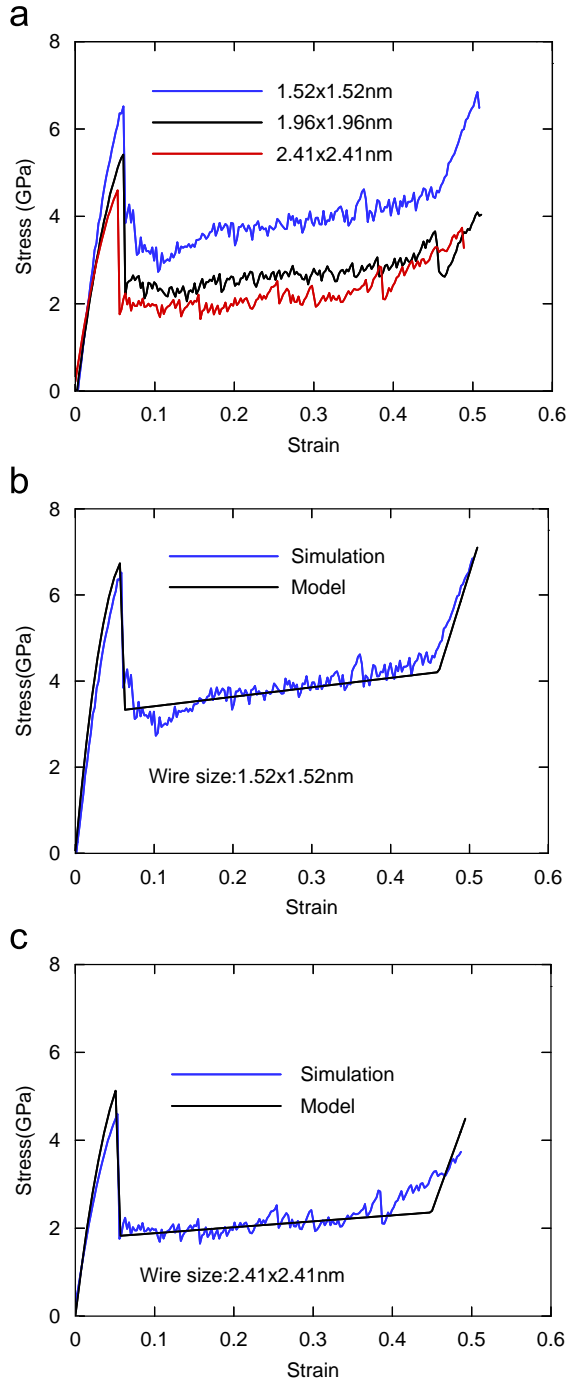| Wire size (nm)	ε_s	σ_y (GPa)	ε_{110}	σ_{110} (GPa)	ε_f	ε_{100}	σ_{100} (GPa)	σ_{dissip} (GPa)
1.52×1.52	0.059	6.52	0.0112	2.20	0.459	0.0322	2.68	1.3
1.96×1.96	0.059	5.41	0.0116	1.81	0.459	0.0317	2.29	0.7
2.41×2.41	0.052	4.60	0.0088	1.35	0.449	0.0247	1.74	0.6

Fig. 17. Size effects: (a) the stress–strain behaviors of $\langle 1\,1\,0 \rangle/\{1\,1\,1\}$ Cu wires of different sizes at $T = 300\,\mathrm{K}$ obtained from MD simulations, (b) and (c) and Fig. 15(d) show the comparisons of the results of MD simulations with the model predictions for wires of sizes of 1.52×1.52, 1.96×1.96, and $2.41 \times 2.41\,\mathrm{nm}$, respectively.

Fig. 16(b). The results of the MD simulations on single-phase wires are consistent with those obtained experimentally and through first principle calculations (Dingreville et al., 2005). Similarly, there are significant size effects in the behavior of $\langle 1\,1\,0 \rangle / \{1\,1\,1\}$ wires with lattice reorientation. Specifically, both the yield stress σ_y and the stresses during lattice reorientation decrease with increasing wire size, as shown in Table 2 and Fig. 17. The model predictions show excellent agreement with the MD simulation results for wires of different sizes. Moreover, the model provides a concrete explanation of why this behavior is size-dependent.

First, the size dependence of σ_y is primarily due to the surface-stress-induced compressive stress in the core of the wire without external loading, as discussed in Section 3.2. Under tensile loading conditions, the externally applied stress first needs to overcome the internal compressive stress and then cause yielding (Diao et al., 2004b; Gall et al., 2004). Since the magnitude of the surface-stress-induced compressive stress decreases with increasing wire size, the overall tensile yield stress decreases with increasing wire size.

Second, the stress component σ_e at phase-equilibrium is primarily determined by the elastic properties of the single-phase wires. Since both $\langle 1\,1\,0 \rangle / \{1\,1\,1\}$ and $\langle 0\,0\,1 \rangle / \{1\,0\,0\}$ single-phase wires are stiffer at smaller sizes, σ_e is higher in smaller wires. On the other hand, according to Eq. (47), σ_{dissip} is proportional to $\Delta u = \Delta U / V_0$, where ΔU is the energy dissipated during the nucleation, propagation and annihilation of a single partial dislocation. In bulk materials, energy dissipation may depend on the path a dislocation travels, because the dislocation interacts with defects such as other dislocations, voids, interstitials, or grain boundaries. The small nanowires here are defect-free other than the single propagating dislocation at hand. As a result, ΔU is the energy difference corresponding to a peak and a valley on the strain energy curve in Fig. 12(a). This difference is associated only with the structure of the single dislocation and is therefore essentially independent of the size of the wire. Since ΔU is the same in wires of different sizes, σ_{dissip} is inversely proportional to the wire volume. Hence, σ_{dissip} is higher in smaller wires due to smaller volumes. Therefore, the stress during lattice reorientation decreases with increasing wire sizes because both σ_e and σ_{dissip} decrease with increasing wire sizes.

6. Conclusions

Our previous research revealed that single-crystalline metal (Cu and Ni) nanowires show a novel SME and pseudoelastic behavior due to a reversible lattice reorientation driven by the high surface-stress-induced internal stress at the nanoscale. In this study, a continuum model is developed to characterize the tensile behavior of these shape memory metal nanowires with a focus on the unique lattice reorientation. Specifically, the lattice reorientation initiates when the $\langle 1\,1\,0 \rangle / \{1\,1\,1\}$ wire reaches its elastic limit and a dislocation is nucleated. Two factors combine to determine the deformation mechanism and the nucleation event. First, there are two competing slip systems under the loading condition: $\langle 1\,1\,1 \rangle / \{1\,1\,0\}$ and $\{1\,1\,1\} / \langle 1\,1\,2 \rangle$, associated with the nucleation of a full dislocation and a Shockley partial dislocation, respectively. A CRSS analysis shows that the $\{1\,1\,1\} / \langle 1\,1\,2 \rangle$ slip systems are more favorable. The Schmid factor for the $\{1\,1\,1\} / \langle 1\,1\,2 \rangle$ slip system is larger than the zero Schmid factor associated with the $\{1\,1\,1\} / \langle 1\,1\,0 \rangle$ slip system (the loading direction is perpendicular to the Burgers vector of the full dislocation). Second, atoms at the sharper inter-facet edges constitute a weaker spot for the nucleation of a partial dislocation. After partial dislocation nucleation, the partial glides

across the wire and forms a coherent twin, separating the $\langle 1\,1\,0 \rangle/\{1\,1\,1\}$ phase and the new $\langle 0\,0\,1 \rangle/\{1\,0\,0\}$ phase. The twin boundary propagates along the wire axis as the lattice reorientation proceeds.

Relying upon the first law of thermodynamics, we have decomposed the lattice reorientation process into two parts: a reversible smooth transition between metastable phase-equilibrium states and an irreversible, dissipative twin boundary propagation process. The smooth transition between static metastable states is modeled within the framework of strain energy functions with multiple local minima. Specifically, at any given strain, the wire adopts the configuration with minimum strain energy while the kinematics constraints and force balance are satisfied. Numerical results show that the stress and strain states in either phase are constant during lattice reorientation. Hence, the elongation of the wire is solely accommodated by the transformation from the $\langle 1\,1\,0 \rangle/\{1\,1\,1\}$ to the $\langle 0\,0\,1 \rangle/\{1\,0\,0\}$ phase. The force is continuous within each phase and across the phase interface. However, the stresses in the two phases are not the same because of the different cross-sectional areas. The slow increase of the total stress during lattice reorientation is due to the increase of the volume fraction of the higher-stress phase.

The dissipative nature of the lattice reorientation is due to the ruggedness of the strain energy curves associated with dislocation nucleation, glide, and annihilation during twin boundary propagation. Each time a dislocation is nucleated and annihilated, the difference in the strain energies between the unstable state and phase-equilibrium state is dissipated. The energy dissipation increases proportionally to the total strain. Therefore, the stress component associated with dissipation is constant at a given temperature. Its magnitude is lower at higher temperatures because thermal fluctuations facilitate dislocation nucleation.

The model captures the major characteristics of the unique behavior due to lattice reorientation and accounts for the size and temperature dependences, yielding results that were shown to be in excellent agreement with the results of MD simulations. The temperature dependence primarily arises from the fact that thermal fluctuations facilitate overcoming the energy barriers for dislocation nucleation. Therefore, the yield stress and the transformation stress during lattice reorientation decrease with increasing temperature. The size dependence of the yield and lattice reorientation stresses is primarily associated with the size dependence of the elastic behaviors of the two single-phase wires. For both $\langle 1\,1\,0 \rangle/\{1\,1\,1\}$ and the $\langle 0\,0\,1 \rangle/\{1\,0\,0\}$ wire configurations, smaller wires are stiffer. Therefore, the yield stress and the transformation stress during lattice reorientation decrease with increasing wire sizes.

Acknowledgments

References

Abeyaratne, R., Kim, S.-J., 1994. A one-dimensional continuum model for shape-memory alloys. Int. J. Solids Struct. 31, 2229–2249.

Abeyaratne, R., Knowles, J.K., 1991. Kinetic relations and propagation of phase boundaries in solids. Arch. Rat. Mech. Anal. 114, 119–154.

Abeyaratne, R., Knowles, J.K., 1993. A continuum model of a thermoelastic solid capable of understanding phase transitions. J. Mech. Phys. Solids 41, 541–571.

Abeyaratne, R., Vedantam, S., 2003. A lattice-based model of the kinetics of twin boundary motion. J. Mech. Phys. Solids 51, 1675–1700.

Abeyaratne, R., Bhattacharya, K., Knowles, J.K., 2001. In: Nonlinear Elasticity: Theory and Applications. Cambridge Univercity Press, Cambridge.

Cammarata, R.C., Trimble, T.M., Srolovitz, D.J., 2000. Surface stress model for intrinsic stresses in thin films. J. Mater. Res. 1511, 2468–2474.

Diao, J., Gall, K., Dunn, M.L., 2004a. Surface stress driven reorientation of gold nanowires. Phys. Rev. B 70, 075413.

Diao, J., Gall, K., Dunn, M.L., 2004b. Yield strength asymmetry in metal nanowires. Nano Lett. 410, 1863–1867.

Dingreville, R., Qu, J., Cherkaoui, M., 2005. Surface free energy and its effect on the elastic behavior of nano-sized particles, wires and films. J. Mech. Phys. Solids 53, 1827–1854.

Dumitrica, T., Hua, M., Yakobson, B.I., 2006. Symmetry-, time-, and temperature-dependent strength of carbon nanotubes. Proc. Nat. Acad. Sci. USA 10316, 6105–6109.

Gall, K., Diao, J., Dunn, M.L., 2004. The strength of gold nanowires. Nano Lett. 412, 2431–2436.

Kondo, Y., Takayanagi, K., 1997. Gold nanobridge stabilized by surface structure. Phys. Rev. Lett. 7918, 3455–3458.

Liang, W., Zhou, M., 2004. Response of copper nanowires in dynamic tensile deformation. J. Mech. Eng. Sci. 2186, 599–606.

Liang, W., Zhou, M., 2005. Pseudoelasticity of single crystalline Cu nanowires through reversible lattice reorientations. J. Eng. Mater. Technol. 1274, 423–433.

Liang, W., Zhou, M., 2006. Atomistic simulations reveal shape memory of fcc metal nanowires. Phys. Rev. B 73, 115409.

Liang, W., Zhou, M., Ke, F., 2005. Shape memory effect in Cu nanowires. Nano Lett. 510, 2039–2043.

Liu, Z., Bando, Y., 2003. A novel method for preparing copper nanorods and nanowires. Adv. Mater. 153, 303–305.

Liu, Z., Yang, Y., Liang, J., Hu, Z., Li, S., Peng, S., Qian, Y., 2003. Synthesis of copper nanowires via a complex-surfactant-assisted hydrothermal reduction process. J. Phys. Chem. B 107, 12658–12661.

Meyers, C., 1984. Mechanical Metallurgy Principle and Applications. Printice-Hall Inc., Englewood Cliffs, NJ.

Mishin, Y., Farkas, D., Mehl, M.J., Papaconstantopoulos, D.A., 1999. Interatomic potentials for monoatomic metals from experimental data and ab initio calculations. Phys. Rev. B 595, 3393–3407.

Mishin, Y., Mehl, M.J., Papaconstantopoulos, D.A., Voter, A.F., Kress, J.D., 2001. Structural stablility and lattice defects in copper: ab initio, tight-binding, and embedded-atom calculations. Phys. Rev. B 63, 224106.

Otsuka, K., Wayman, C.M. (Eds.), 1998. Shape Memory Materials. Cambridge University Press, New York.

Park, H.S., Ji, C., 2006. On the thermomechanical deformation of silver shape memory nanowires. Acta Mater. 5410, 2645–2654.

Park, H.S., Gall, K., Zimmerman, J.A., 2005. Shape memory and pseudoelasticity in metal nanowires. Phys. Rev. Lett. 95, 255504.

Parker, S.P. (Ed.), 2002. McGraw-Hill Dictionary of Scientific and Technical Term, Sixth ed. McGraw-Hill Professional, New York.

Plimpton, S.J., 1995. Fast parallel algorithms for short-range molecular dynamics. J. Comp. Phys. 117, 1–19.

Puglisi, G., Truskinovsky, L., 2002. A mechanism for transformational plasticity. Continuum Mech. Thermodyn. 14, 437–457.

Rodrigues, V., Ugarte, D., 2003. Structural study of metal nanowires. In: Wang, Z.L. (Ed.), Nanowires and Nanobelts: Materials, Properties and Devices. Springer, New York, pp. 177–209.

Schuh, C.A., K.Mason, J., Lund, A.C., 2005. Quantitative insight into dislocation nucleation from high-temperature nanoindentation experiment. Nat. Mater. 4, 617–621.

Streitz, F.H., Cammarata, R.C., Sieradzki, K., 1994. Surface-stress effects on elastic properties. I. Thin metal films. Phys. Rev. B 49, 10699–10706.

Trushin, O., Granato, E., Ying, S.C., Salo, P., Ala-Nissila, T., 2002. Minimum energy paths for dislocation nucleation in strained epitaxial layers. Phys. Rev. B 65, 241408–241414.

Truskinovsky, L., Vainchtein, A., 2003. Peierls–Nabarro landscape for martensitic phase transitions. Phys. Rev. B 6717, 172103–172114.

Truskinovsky, L., Vainchtein, A., 2004. The origin of nucleation peak in transformational plasticity. J. Mech. Phys. Solids 526, 1421–1446.

Vainchtein, A., Rosakis, P., 1999. Hysteresis and stick–slip motion of phase boundaries in dynamic models of phase transitions. J. Nonlinear Sci. 9, 697–719.